A critical appraisal of water table depth estimation: Challenges and opportunities within machine learning

Joseph Janssen[1], **Ardalan Tootchi**[1], **and Ali A. Ameli**[1]

[1]Department of Earth, Ocean, and Atmospheric Sciences, University of British Columbia, Vancouver, BC, Canada

Abstract

Fine-resolution spatial patterns of water table depth (WTD) can inform the dynamics of groundwater-dependent systems, including ecological, hydrological, and anthropogenic systems. Generally, a large-scale (e.g., continental or global) spatial map of static WTD can be simulated using either physically-based (PB) or machine learning-based (ML) models. We construct three fine-resolution (500 m) ML simulations of WTD, using the XGBoost algorithm and more than 20 million real and proxy observations of WTD, across the United States and Canada. The three ML models were constrained using known physical relations between WTD's drivers and WTD and were trained by sequentially adding real and proxy observations of WTD. We interpret the black box of our physically constrained ML models and compare it against available literature in groundwater hydrology. Through an extensive (pixel-by-pixel) evaluation, we demonstrate that our models can more accurately predict unseen real and proxy observations of WTD across most of North America's ecoregions compared to three available PB simulations of WTD. However, we still argue that large-scale WTD estimation is far from being a solved problem. We reason that due to biased and untrustworthy observational data, the misspecification of physically-based equations, and the over-flexibility of machine learning models, our community's confidence in ML or PB simulations of WTD is far too high and verifiably accurate simulations of WTD do not yet exist in the literature, particularly in arid high-elevation landscapes. Ultimately, we thoroughly discuss future directions that may help hydrogeologists decide how to proceed with WTD estimations, with a particular focus on the application of machine learning.

Keywords: Machine learning, physically-based models, Groundwater, Water Table Depth, North America, Ecoregions, Model uncertainty, Observation uncertainty

1 Introduction

Groundwater is the most abundant source of freshwater on Earth, with an important influence on above-ground processes (Gleeson et al., 2016). Groundwater affects water quantity and quality in streams (Miguez-Macho & Fan, 2012; G. A. Ali et al., 2011), lakes (Vaheddoost & Aksoy, 2018; S. Xu et al., 2021; Ameli & Craig, 2014), and wetlands (Ameli & Creed, 2019, 2017), and regulates the behaviour of ecological and human-centric systems (Siebert et al., 2010). In riverine ecosystems, groundwater provides critical water supplies to plants in arid riparian and non-riparian areas, without which trees and plants would quickly deteriorate in drought conditions (Kibler et al., 2021; G. Xu et al., 2022). The central property of groundwater at a particular location is the water table depth (WTD), defined as the depth below which the ground becomes fully saturated with water. The spatial pattern of WTD determines the velocity and direction of groundwater movement (Freeze & Cherry, 1979), whether or not the roots of trees can uptake water (Tai et al., 2018; Cooper et al., 2003; Schook et al., 2022), the celerity of the rainfall-streamflow response (Scaini et al., 2018), the nonlinearity of stormflow and baseflow generation (G. A. Ali et al., 2011; Detty & McGuire, 2010; Kim et al., 2004; Li & Ameli, 2023), and the severity of lake and stream gain or loss (Jasechko et al., 2021; Freund et al., 2023). Static WTD, which is the main focus of this paper, is defined as the long-term non-transient water table depth between recharge events in a given aquifer. The static WTD can vary by several orders of magnitude from one location to another due to large spatial variations in topographic, geological, soil, land cover, and climatic attributes. Fine-resolution

Corresponding author: Joseph Janssen, joejanssen@eoas.ubc.ca

spatial estimates of WTD, especially at continental and global scales, can inform (1) the spatial heterogeneity in typical (or long-term) hydrologic processes within and across catchments, (2) the delineation of stable catchment boundaries (Hinton et al., 1993), (3) the overall gaining or losing status of surface water bodies connected to groundwater systems, and (4) the spatial extent of drought and flood vulnerabilities (Brooks et al., 2015; Smith & Majumdar, 2020; Gleeson et al., 2021).

Previous studies have attempted to simulate WTD at local, regional, national, and global scales using various methods. For example, in an aquifer near Toronto, Canada, Desbarats et al. (2002) used a geostatistical method (kriging with external drift) to estimate the WTD at 90m resolution using the information of elevation and topographic wetness index. Kollet and Maxwell (2008) and Tran et al. (2022) used ParFlow, a physically-based groundwater model, to simulate WTD in a catchment in Oklahoma and Colorado, respectively. Further, national-scale simulations of WTD have been made by R. Maxwell et al. (2015) using ParFlow (across a large portion of the United States with 1 km resolution), by Koch et al. (2021) using a machine learning algorithm called catboost (across Denmark with 10 m resolution), by Ben-Salem et al. (2023) using kriging (across Spain and Portugal with 4 km resolution), and by Koch et al. (2019) using random forests to simulate winter-time WTD in Denmark with 50 m resolution. One of the most prominent examples of a global simulation of WTD was conducted by Fan et al. (2013), who used a physically-based model to develop a 1 km grid of WTD for the entire planet. Another estimation of global WTD was made by de Graaf et al. (2017), as an extension of their earlier work (de Graaf et al., 2015). This was the first global-scale transient model, and estimates were made via PCR-GLOBWB and MODFLOW at a 10 km resolution. Building on global-scale WTD simulations, Reinecke, Foglia, Mehl, Trautmann, et al. (2019) developed a global gradient-based groundwater model for the hydraulic head. They proceeded to compare the simulations of de Graaf et al. (2015), Fan et al. (2013), and R. Maxwell et al. (2015) with a set of global observations, finding that the predictions made by Fan et al. (2013) and R. Maxwell et al. (2015) better fit to observed hydraulic head. Ben-Salem et al. (2023) further compared the simulations of de Graaf et al. (2015), Fan et al. (2013), and Reinecke, Foglia, Mehl, Trautmann, et al. (2019) with well observations from Portugal and Spain. In contrast to Reinecke, Foglia, Mehl, Trautmann, et al. (2019), Ben-Salem et al. (2023) concluded that the simulations of de Graaf et al. (2015) better matched their set of observations compared to the simulations of Fan et al. (2013) and Reinecke, Foglia, Mehl, Trautmann, et al. (2019).

Attempts to simulate national or global-scale WTD have typically fallen into two categories: (1) physically-based models and (2) machine learning models, each containing notable shortcomings. Physically-based numerical methods are flexible enough to incorporate spatiotemporal variations in recharge, heterogeneous soil properties, and time-varying boundary conditions. However, they may only make valid predictions for locations that perfectly follow a long list of assumptions under which the model was built, with the scale being one of the most important and often contradicted assumptions (Herrera et al., 2022). Darcy's law, the backbone of physically-based models, requires a fine grid discretization of physically-based models (e.g., less than 1 meter) to be reliably implemented. Hence, the reliable and robust application of physically-based models at scales larger than regional ones is computationally costly. Without major breakthroughs in computer processor speeds, running a physically-based model at such a fine resolution for country-to-global scales will continue to be computationally infeasible (Koch et al., 2021). This may explain why available large-scale physically-based simulations of WTD generally have coarse resolutions (e.g., 1 km in Fan et al. (2013) and 10 km in de Graaf et al. (2015)).

The vertical extent of the simulation domain in physically-based models can also limit the accuracy with which WTD can be estimated. R. Maxwell et al. (2015) stated that one of the main limitations of their physically-based model developed to estimate WTD across a large portion of the USA was specifying the lower model boundary at 102 m. The lack of knowledge on the proper location of a model's lower boundary condition leads to possible underestimation of WTD magnitude in dry and mountainous regions, while it is known that actively circulating groundwater can be as deep as 200 meters in mountainous regions (Condon et al., 2020). Furthermore, numerical instabilities often cause convergence issues, leading to unrealistic WTD simulations by physically-based models (Herrera et al., 2022). Unstable predictions of hydraulic heads are commonly observed in physically-based models, especially in dry and mountainous regions, which cover a large portion of North America and the globe (Reinecke, Foglia, Mehl, Herman, et al., 2019). Moreover, physically-based models depend highly on parameters such as hy-

draulic conductivity, which could be challenging to estimate at global scales (de Graaf et al., 2015; R. Maxwell et al., 2015; Ofterdinger et al., 2014). From extensive testing, Reinecke, Foglia, Mehl, Herman, et al. (2019) and Ofterdinger et al. (2014) found that the WTD is extremely sensitive to small changes in hydraulic conductivity levels.

Machine learning methods could resolve some of the previously mentioned shortcomings of physically-based models but can also create additional limitations. Machine learning models (1) do not rely on uncertain and scale-dependent physically-based assumptions, (2) do not lead to numerical instabilities, (3) are pronouncedly less computationally intensive, and (4) can flexibly down-weight important variables with high measurement uncertainty such as hydraulic conductivity. However, these models strongly rely on observational data, which are very sparse and have considerable bias and uncertainty. The black-box nature (and the lack of physical realism) of typical machine learning models, together with sparse, biased, and uncertain observational data, may reduce the chance of learning groundwater systems' *true* functional (or structural) behaviour. This is critically required to generalize and robustly extrapolate WTD estimates beyond available sparse observations. Poor measurement quality, sparse well drilling in certain areas, unknown impacts of external and non-natural drivers such as pumping, and vertical gradients due to having an unknown mix of measurements from confined, unconfined, and perched aquifers may lead to spurious relationships in WTD datasets that the machine learning model will hopelessly follow (Koch et al., 2021).

With the advent of technologies such as geophysical surveys and remote sensing products, we are now amassing fine-resolution globally available data that equally cover different types of landscapes and could (in)directly inform WTD simulations. One notable example includes a fine-resolution (e.g., 30 m) satellite-based map of the probability of surface water occurrence (Pekel et al., 2016), obtained through merging time-varying satellite information, which could inform the permanency of hydraulic connection between groundwater and surface water systems, and ultimately inform WTD at a fine resolution. These types of fine-resolution proxy data have rarely been used in developing (or validating) machine learning or physically-based groundwater models. Furthermore, machine learning models are becoming more flexible in incorporating physical-based information, which can be used to minimize the lack of physical realism of such models.

Another obstacle in the way of obtaining a robust and trustworthy large-scale simulation of WTD is the lack of *verifiability* of physically-based and machine learning-based groundwater models. For example, R. Maxwell et al. (2015) verified their large-scale simulation of WTD by comparing the simulated and observed hydraulic heads, where the observed hydraulic head was calculated using the observed WTD and elevation. Later, de Graaf et al. (2017) and de Graaf et al. (2015) measured the R^2 of simulated versus observed hydraulic head in sediment basins versus mountain ranges. In fact, almost all large-scale studies that used physically-based models to simulate WTD have verified their model by comparing hydraulic head simulations with hydraulic head observations rather than directly evaluating simulated versus observed WTD (Fang et al., 2019). Given the dominance of elevation in explaining the spatial variability of the hydraulic head, almost perfect corroboration between the observed and simulated hydraulic head does imply that the model performance is acceptable in simulating WTD, nor does it ensure that the model structure replicates the true structure of the groundwater systems. Indeed, large R^2 between observed and simulated hydraulic heads (e.g., > 0.99) may imply $R^2 < 0$ between observed and simulated WTD (see Section 5.2). In contrast to physically-based models, when machine learning models were used to simulate WTD, such as in Koch et al. (2019), Koch et al. (2021), and Ma et al. (2024), the performance of the model was verified by comparing the modelled versus observed WTD among test set observations. Test set performance indicates the accuracy of WTD simulations at *unseen* observations. Normally, this reflects how much we can trust the machine learning simulations of WTD in regions with no WTD observations, however due to pervasive observational biases (see Section 5.1), this may not be the case, thus verifiability is diminished. Beyond just comparing observations with simulations, we will also discuss the importance of testing how well the model learns the groundwater systems' true functional (or structural) behaviour.

In this paper, we estimate a fine-resolution (500 m) spatially continuous map of (static) WTD in unconfined aquifers across the United States and Canada. We leverage the computational efficiency and flexibility of machine learning while incorporating physical boundary conditions known to constrain ground-

water models and functional relationships known to control WTD. In doing so, we use (1) more than 9 million real observations of WTD collected at more than 900,000 observational wells across the United States and Canada, (2) a physically-constrained XGBoost machine learning model, and (3) more than 12 million satellite-based proxy observations, to further enhance the physical consistency of the machine learning model. Using the XGBoost machine learning model and subsets of real and proxy observations, we provide three setups of simulated WTD across the study region. In these three setups, the training data used to develop each machine learning model increases from setup one to setup three by sequentially adding satellite-based proxy observations to real observations of WTD. In doing so, we showcase the consequences of using proxy observations in simulating WTD. Using unseen real and proxy observations of WTD, we then evaluate and compare our three machine learning simulations of WTD across ten ecoregions of North America with three physically-based simulations of WTD. This analysis indicated where different machine learning and physically-based simulations corroborate each other's conclusions and where each simulation followed currently available observations. Finally, we critically appraise our three sets of machine learning-based WTD simulations alongside the three physically-based simulations of WTD to illustrate current issues related to model structural uncertainties, simulation verifiability, and observational uncertainties, while also revealing future directions for model development, data collection, and experimental analysis.

2 Data

2.1 Input Variables Used to Develop Machine Learning Models

2.1.1 Climate data

Climatic attributes and conditions influence recharge intensity and timing, which are among the main drivers of regional water table depth (de Graaf et al., 2017; R. Maxwell et al., 2015; Moeck et al., 2020). Here, we calculated the long-term average values of climatic attributes, including precipitation, temperature, temperature of the month of January, rainfall intensity, maximum snow water equivalent (SWE), snow fraction, aridity index, and precipitation excess for the period between 1979-2009, which covers the time from which the bulk of real and proxy WTD observations are available. January temperature was used in addition to average temperature, as previous studies showed that winter temperature affects soil frost and, ultimately, WTD properties (Fan et al., 2013). To quantify long-term average precipitation, temperature, January temperature, rainfall intensity, and snow fraction, we used the EMDNA dataset (Tang et al., 2021), which provides daily precipitation and temperature at a resolution of 0.1 degrees. The long-term average snow fraction was calculated as the sum of snowfall (precipitation during days with below zero temperature) over the sum of precipitation. Rainfall intensity was calculated as the average rainfall intensity (mm/day) across days with over 1 mm of rain.

Long-term average values of potential evapotranspiration, actual evapotranspiration, and maximum snow water equivalent were estimated using the TerraClimate dataset (Abatzoglou et al., 2018) at a resolution of 0.04 degrees. We combined gridded precipitation from EMDNA and potential evapotranspiration from TerraClimate to calculate the gridded continent-wide aridity index values as the ratio between potential evapotranspiration and precipitation. Gridded precipitation excess was also calculated for North America as precipitation from EMDNA minus actual evapotranspiration from TerraClimate. The long-term average maximum snow water equivalent (SWE) was calculated as yearly maximum SWE from TerraClimate, averaged across all years. All climatic attributes were down-scaled to our target resolution (500 m).

2.1.2 Topography

Conceptually, in most mountainous landscapes, the water table may follow an extremely damped version of topography (Desbarats et al., 2002; Moreno et al., 2015). Indeed, in mountainous regions, water tables are often observed and simulated to be deep (de Graaf et al., 2017). This is not only due to lateral groundwater flow seeking equilibrium but also due to decreased recharge at higher elevations (Moeck et al., 2020). Further, flat topography encourages discharge formations such as rivers, wetlands, and lakes, while mountainous terrains usually correspond to low-storage areas (Moeck et al., 2020). At the same

time, precipitation increases with elevation while evapotranspiration tends to decrease. Hence, topography is one of the primary drivers of WTD, with the complex relationship between topography and groundwater recharge (and WTD) depending on how topography interacts with precipitation, evapotranspiration, and geological formations (Moeck et al., 2020). Machine learning may provide a strong foundation for exploring and simulating such a complicated relationship. Here, we used different topographical attributes which are known to control recharge and WTD. These attributes include elevation, slope, and topographic index. To cover the entire extent of the United States and Canada, we merged two elevation datasets. SRTM15+ (Tozer et al., 2019) was used for zones below 60 degrees North, while GTOPO30 (Daac, 2004) was used for higher latitudes. The former dataset is available at our target resolution (500 m), while GTOPO30 is a global digital elevation model (DEM) with a grid spacing of 30 arc seconds (approximately 1 km) and had to be converted to our target resolution. Using the merged elevation dataset and GIS spatial analysis tools, terrain slope was calculated in degrees. Marthews et al. (2015) created a global 500 m resolution dataset of Topographic Index (TI), the index that was introduced by K. J. Beven and Kirkby (1979), to characterize the topographic control on the distribution of water. This TI dataset was directly used in our model without any preprocessing.

2.1.3 Geology

Gleeson et al. (2014) developed global maps of bedrock permeability and porosity, two key properties for understanding groundwater hydraulics (Moeck et al., 2020). In our study, bedrock permeability and porosity were initially used as input data to the machine learning models to inform the geological characteristics of the shallow subsurface. However, our results showed zero importance for these two attributes, meaning that our machine learning models did not use the information of these two attributes to simulate the spatial pattern of WTD at local to regional scales. This could be due to the very small variations of these two attributes across our study region. Instead, incorporating hydraulic characteristics of deep soil, which will be introduced in the next section, to a large extent, emulated deeper subsurface hydraulics.

2.1.4 Soil data

While climate is the driver of overall catchment recharge, soil hydraulic properties control the partitioning between subsurface vertical infiltration (and recharge) and lateral flows (R. Maxwell et al., 2015; Moeck et al., 2020). Low soil hydraulic conductivity prevents water from entering the subsurface, encouraging the input water to exit the catchment via overland flow instead of contributing to soil moisture or aquifer recharge (R. Maxwell et al., 2015; Moeck et al., 2020). de Graaf et al. (2015) argues that the soil saturated hydraulic conductivity is one of the most dominant controls of WTD, where higher conductivity lowers the water table and enhances regional flow. Soil thickness (and soil porosity) may also impact groundwater placement (de Graaf et al., 2015).

The Soilgrids dataset (Poggio et al., 2021) is a comprehensive global-scale information system providing high-resolution soil property maps for various depths and soil layers. The dataset covers a wide range of soil properties, including sand, silt, and clay fractions, organic carbon content, bulk density, depth to bedrock (or soil thickness), and more at a spatial resolution of approximately 250 meters. To characterize hydraulic properties, the clay, silt, and sand fractions within the first 15 cm depth were aggregated to a resolution of 500 m. Similarly, the available data of clay, silt, and sand fractions below 1 m were aggregated to a resolution of 500 m to present the hydraulic properties of a relatively deeper portion of the Earth's surface material. These aggregated fractions at two different vertical positions were then utilized as input parameters for the machine learning groundwater models. Furthermore, the gridded depth to bedrock data was gathered from Dai et al. (2019), converted to 500 m resolution, and used as an additional soil-related input to our machine learning models.

2.1.5 Land cover

Vegetation plays a critical role in determining water input partitioning and ultimately groundwater recharge (Allen et al., 1998; Moeck et al., 2020). Different types of vegetation have varying rates of transpiration, which is the process by which plants take up and release water into the atmosphere through

the stomata on leaves. For example, a forested area with tall trees may have a higher rate of transpiration than a grassland, leading to a higher rate of evapotranspiration. This variation in transpiration and evaporation rates will affect the amount of water available to recharge the groundwater system, ultimately affecting the water table's depth. Changes in land use can impact recharge rates even if the climatic conditions remain the same, as noted by DeFries and Eshleman (2004); Minnig et al. (2018).

The Collection of Moderate Resolution Imaging Spectroradiometer (MODIS) Land Cover Dynamics Product, called MCD12Q, provides global land cover and phenology metrics at 500-meter spatial resolution. MCD12Q dataset includes annual land cover maps with 17 classes, including 11 natural vegetation classes, three human-altered classes, and three non-vegetated classes. In this study, MCD12Q's land cover map of the year 2000 was acquired and reclassed. Different forested land cover classes were combined to form one unique forested land cover class. Similarly, different shrubland classes and grassland classes were combined to form one unique shrubland class and grassland class, respectively. This led to a total of 7 land cover classes which were used as categorical inputs to the machine learning-based groundwater models. The classes selected for this analysis were chosen based on established findings on the relationships between land cover and groundwater recharge rate (and ultimately WTD) (Owuor et al., 2016; Scanlon et al., 2005; Mohan et al., 2018; Zhang & Schilling, 2006).

2.2 Real Observations of Water Table Depth

Water well observational information in the United States and Canada was compiled from national organizations and provincial databases. Water well observational information in the United States was downloaded from USGS's database on "Groundwater levels for the Nation" (`https://nwis.waterdata.usgs.gov/nwis/gwlevels`). In Canada, historic well reports are documented and made available for public use in most provinces. However, these datasets are not often compatible with each other in terms of measurement attributes, units, and accuracy. Details of provincial databases, data format, and web links for each province are provided in the Supplement. A total of 9.6 million observations collected between 1852 and 2022 (with the majority collected between 1979-2009) were compiled at 905,371 observational wells across the USA and Canada. When multiple observations over time in a given well were present, the minimum value of WTD was taken to obtain one representative observation for the given well. This treatment could enhance the chance of obtaining representative static WTD observations, which are minimally influenced by pumping. Moreover, when converting point-based WTD observations to the target resolution of our study (i.e. 500 m pixels), there were instances, especially across flat agricultural lands, where two or more observational wells were situated within a single pixel. In such cases, the median WTD was designated as the pixel's representative observation of WTD. Figure 1 shows (in red) the 500 m resolution pixels with available representative observations of WTD across the Prairie Pothole region of North America and the Mississippi River Basin.

2.3 Proxy Observations of Water Table Depth

2.3.1 Occurrence of surface water inundation connected to groundwater systems

Persistent water inundation on the Earth's surface is a strong indicator of hydraulic connection between surface water and the surrounding groundwater system and thus could exhibit the location of the water table (de Graaf et al., 2017; Fan et al., 2013; R. Maxwell et al., 2015; Koch et al., 2019). The static water table depth can be considered to be close to zero at the interior and shoreline of persistent rivers, streams, wetlands, potholes, and lakes (de Graaf et al., 2017). Pekel et al. (2016) used more than three million Landsat satellite images to record the months (including summer) when water was present on the ground, between 1984 and 2015. They developed a probabilistic metric, Water Occurrence Percentage (WOP), which reflects the percentage of time at a given 30 m x 30 m pixel when water was present on the ground surface. The metric varies between 0 (no water) and 100 (permanent water), with values in between reflecting the intermittent presence of water. This milestone database was used in our study to develop two sets of WTD proxy observations. The first set of proxy observations reflects the permanently wet interior pixels of (typically small) surface water bodies and is used in our study as one line of evidence to evaluate and compare the performance of three machine learning and three physically-based simulations of WTD. The second set of proxy observations reflects the shorelines of surface water bodies of

different sizes and is used in our study to train two setups of machine learning-based models of WTD. Note that there is no overlap between the first and second sets of pixels utilized for the first and second objectives. Consequently, the pixels that evaluate the performance of six machine learning and physically-based models are mutually exclusive from those used for training the machine learning models.

First, we aggregated the 30 m resolution surface water inundation database to our target resolution (500 m). During this aggregation process, the representative WOP at each 500 m resolution pixel was calculated as the maximum WOP among all WOPs of the original 30 m resolution pixels. Similar to the original 30 m resolution database, the pixel's representative WOP at our target resolution ranged from 0 to 100.

The first set of proxy data, aimed at delineating the permanently wet interior pixels of surface water bodies, was compiled by identifying pixels where surface water inundation was consistently detected over a specific temporal threshold. Pixels experiencing water inundation for more than 95% of the time (i.e. WOP>95%) were delineated and merged. Then, we used the HydroLAKES dataset (Messager et al., 2016), which provides polygonal representations of water bodies, to select those pixels which were fully inside water-body polygons. 7,920,475 pixels representing the interior of permanently wet surface water bodies were extracted and used to evaluate the three physically-based and three machine learning models' performances in locating pixels where WTD is expected to be zero (this will be further explained in Section 3.4). HydroLAKES appears to have missed some water features with WOP>95%. Notable examples are thousands of long and stretched water bodies, which may have been missed in surveying conducted to develop the HydroLAKES dataset, due to their narrow widths, restricted access, or other reasons. In such cases, merged pixels with WOP>95% were considered as permanently wet surface water bodies' pixels. Note that visible and near-infrared range images used in Pekel et al. (2016), could have missed some water features, because the light at these frequencies could be impeded by cloud cover, canopy, and ice. To account for this uncertainty, we incorporated an arbitrary error margin of 5%, or the 95% threshold of WOP, to delineate permanently wet pixels. Opting for smaller error margins (e.g., 1-2%) would misrepresent significant lakes, while larger than 5% error margins would pose a risk of overestimating the permanently wet surface water bodies. Therefore, a WOP of 95% was deemed the most appropriate threshold for this part of the study. Furthermore, we only relied on surface water bodies with surface areas between 30 and 80,000 hectares to ensure that a disproportionately large number of pixels were not selected from the interior of very large surface water bodies (e.g. the Great Lakes of North America). Note that excluding interior pixels of large water bodies enhanced the spatial uniformity of pixels, allowing for a fair evaluation and comparison of the models' performance.

The second set of proxy data, aimed at delineating the semi-permanently wet shorelines of surface water bodies, was compiled again by pixel-based WOP values. Pixels meeting the criterion of inundation (WOP>75%) were delineated and merged. Then, the peripheral, non-interior pixels around the groups of merged pixels were identified as the pixels of surface water bodies' shorelines. The selection of the 75% threshold ensured the inclusion of areas beyond the interior of permanently wet surface water bodies that are still experiencing semi-persistent surface water inundation. Peripheral pixels with WOP>75% indicate prolonged surface water inundation with potentially stable soil saturation, allowing the inference of the water table location. Our preliminary analysis showed that choosing a larger threshold of WOP, such as 85-90%, could have excluded a large portion of surface water bodies' shorelines delineated using other datasets (e.g., HydroLakes). On the other hand, opting for smaller thresholds (e.g., 60-50%) risked including ephemerally inundated areas like wave run-up and overland runoff, which have no stable connection to surrounding groundwater systems. The 30 m resolution and the temporal information on surface water inundation provided by Pekel et al. (2016) dataset facilitated the identification of the shorelines of numerous small and/or locally (and semi-permanently) inundated areas, which were not delineated by other available datasets such as HydroLAKES. In the end, 12,167,332 pixels were delineated as the pixels of shorelines of surface water bodies across the study region at a resolution of 500 m. These pixels were considered locations with static WTD equal to zero (i.e. the WTD to be at the land surface). They will be utilized as proxy observations of WTD in developing (i.e. training and validating) two setups of machine learning-based models of WTD, which will be further elucidated in Section 3.3.3. Figure 1 shows (in blue) the delineated locations of surface water body shorelines across the Prairie Pothole region of North America and the Mississippi River Basin at 500 m resolution.

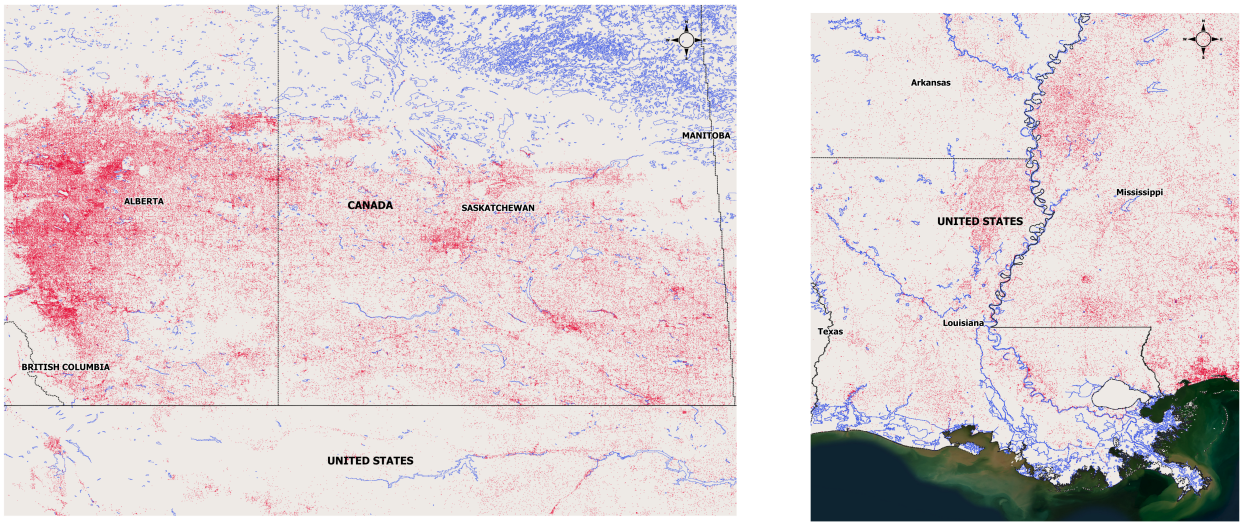

(a) Prairie Pothole Region, Canada

(b) Mississippi, USA

Figure 1: 500 meter resolution pixels showing the locations of the available real observations of WTD (red) and that of the delineated shorelines of surface water bodies (blue), across the Prairie Pothole and Mississippi River Basin regions. Our real observations of WTD and the delineation of the shorelines of surface water bodies extend throughout the entire United States and Canada. But for the sake of simplicity of visualization, we only show these two selected regions with fairly dense observations and delineated shorelines.

2.3.2 Height Above Nearest Drainage

Digital Elevation Models (DEMs) inform the development of numerical descriptors relevant to identifying hydrological processes and WTD (Sivapalan & Kalma, 1995). One of WTD's most relevant DEM-based descriptors is the Height Above Nearest Drainage (HAND) (Nobre et al., 2011; Koch et al., 2019). Using a hydrologically coherent DEM, HAND values were calculated by (1) finding the drainage pixels using DEM-based upslope accumulated area. Drainage pixels are those with above some threshold value of upslope accumulated area. (2) The nearest drainage pixel was found for a given pixel, and their elevational differences were computed to obtain the HAND value for the given pixel. An extensive experimental campaign in northern Brazil by Nobre et al. (2011) showed a strongly positive linkage between the static (non-transient) WTD and HAND values along steep mountainous regions. Indeed, WTD at a given pixel can strongly follow the surface elevation of its local drainage network. In our study, we used the HAND dataset to generate proxy observations of WTD along steep mountainous regions, with limited or completely absent real observations of WTD. The global HAND dataset, originally calculated at a resolution of 3 arc-seconds (Yamazaki et al., 2019), was utilized and resampled to match our study's reference resolution (500 m). Note that a $500m^2$ threshold of upslope accumulated area was used in Yamazaki et al. (2019) in defining the drainage pixels. The use of HAND data as additional proxy observations of WTD for our third setup of machine learning-based simulations will be further explained in Section 3.3.3.

2.4 Previous large-scale simulations of WTD

We compare our three machine learning-based simulations of WTD (see Section 3.3.3) with physically-based simulations by Fan et al. (2013), R. M. Maxwell and Condon (2016), and de Graaf et al. (2015) (data was gathered from De Graaf and Stahl (2022)). Fan et al. (2013) used a simple 1 km gridded Darcy-based numerical scheme to simulate WTD globally. For the top 1 meter of soil, they used available datasets of hydraulic conductivity. They assumed an exponential decay of hydraulic conductivity for deeper ge-

ology and calibrated three parameters using water table depth observations in North American temperate zones. They also calibrated permafrost parameters using observations of wetland extent in Northern USA and Canada. R. M. Maxwell and Condon (2016) generated a 1 km resolution map of WTD across a large portion of the USA, using the ParFlow-CLM model. ParFlow-CLM is a surface-subsurface interaction model that uses 3D Richard's equation for groundwater fluxes. Overland flow is simulated with the kinematic wave equation, while above-ground atmospheric and vegetation processes are simulated with the Common Land Model (CLM). The simulations of R. M. Maxwell and Condon (2016) are uncalibrated, though they use some information about surface water bodies to delineate the model's boundaries. Finally, the global 11 km resolution simulation of WTD from de Graaf et al. (2015) was produced by coupling the land-surface model PCR-GLOBWB with the groundwater model MODFLOW. Each pixel in their coupled model has one canopy layer, two soil layers, and one groundwater layer. Groundwater flux is forced using temperature, potential evapotranspiration, and precipitation, while land cover, soil, and topography conditions are set using globally available datasets. Boundary conditions are set at large lakes and coastlines. Some hydrogeological parameters within the model of de Graaf et al. (2015) were chosen based on how well the simulated hydraulic heads fit the hydraulic heads from piezometer observations. In the remainder of this paper, we refer to studies conducted by de Graaf et al. (2015) as de Graaf's simulation, Fan et al. (2013) as Fan's simulation, and R. M. Maxwell and Condon (2016) as Maxwell's simulation.

2.5 Ecoregions

Ecoregions are defined as areas of the Earth's surface that contain distinct assemblages of natural communities and environmental conditions. They are a way to divide the planet into relatively homogeneous areas based on similarities in climate, geology, topography, vegetation, and wildlife. The United States Environmental Protection Agency (EPA) divides North America into 15 different ecoregions based on the Omernik Ecoregion Framework (Omernik, 1987). The Omernik Ecoregion Framework is widely used by scientists and resource managers to understand and manage diverse natural ecosystems (Gallant, 1989). These 15 ecoregions are: Arctic Cordillera, Tundra, Taiga, Marine West Coast Forest, Eastern Temperate Forest, Great Plains, North American Deserts, Mediterranean California, Southern Semi-Arid Highlands, Temperate Sierras, Tropical Dry Forest, Tropical Rainforest, Western Mountains, Valleys, and Coast Arctic Plains and Mountains. Note that the real observations of WTD were only available within ten ecoregions, and hence in the remainder of the paper, we only use the information of these ten ecoregions (Figure 2). Table 1 reports some statistics regarding these ten ecoregions' climatic, topographic, and soil characteristics. Our paper classified the USA and Canadian lands into ten ecoregions to compare and evaluate (using different lines of evidence) the performance of the three machine learning-based and three physically-based simulations of WTD in different ecoregions of North America.

3 Methods

This paper aims to produce three sets of machine learning-based simulations of WTD (at 500 m resolution) in shallow unconfined aquifers across the USA and Canada. Section 3.1 explains our algorithm to filter out real WTD observations collected in confined aquifers. We then explain the resampling algorithm used to downscale coarse climatic input attributes to our target resolution (Section 3.2). We explain the machine learning methodology, the physically meaningful constraints used to constrain the machine learning models, and the calibration procedures used to develop the three machine learning model setups (Section 3.3). We also explain how the three model setups were developed by gradually adding WTD proxy data to our training set (Section 3.3.3). The evaluation criteria used to evaluate and compare the performances of the three machine learning simulations and the three available physically-based simulations of WTD are discussed in Section 3.4.

3.1 Filtering of real WTD observations

This paper particularly focuses on the simulations of WTD within unconfined aquifers. Hence, we excluded the real well observations potentially collected within confined layers. Here, we leveraged the flag indicating whether the WTD observations came from confined or unconfined aquifers from a sub-

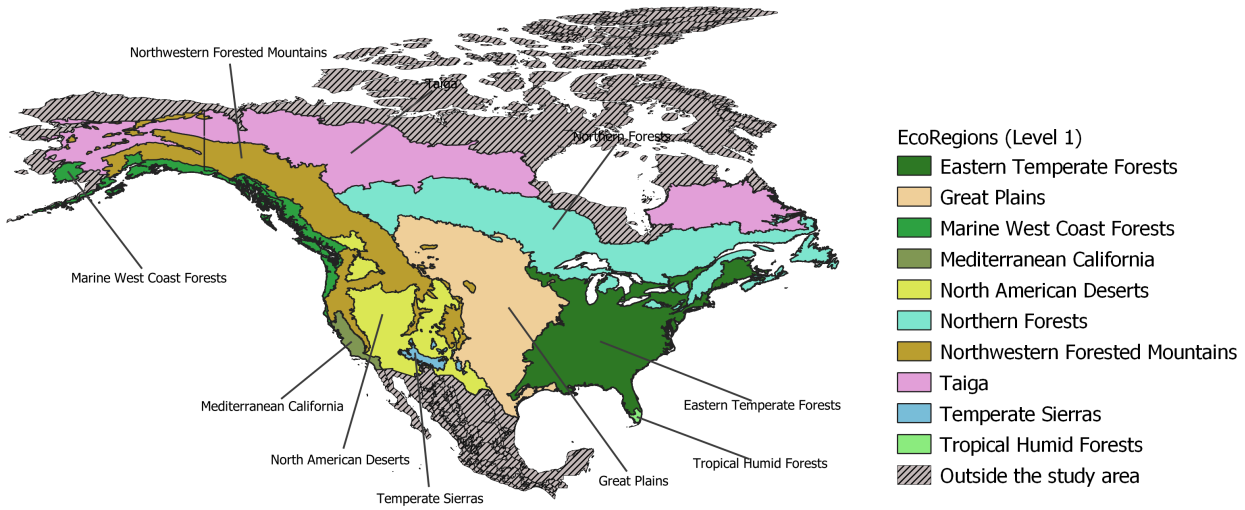

Figure 2: The locations of ten ecoregions along which we compare and evaluate the performance of the three machine learning-based and three physically-based WTD simulations.

set of WTD observational data in the United States and British Columbia in Canada. We explored whether well depth and geologic and climatic characteristics could explain the confined versus unconfined status of the observational data. We could then extrapolate this information to the other observational data where the confined versus unconfined status is unknown, but other characteristics are known. Since the ultimate aim was extrapolation, a powerful yet interpretable model was required. Hence, we employed a non-greedy decision tree algorithm, which provides accurate and interpretable extrapolation, using the *evtree* R package (Grubinger et al., 2014). Inputs to the algorithm include climatic attributes, such as aridity index, precipitation, and snow fraction; geological attributes, such as depth to bedrock; topographical attributes, such as elevation; and well information, such as well depth. We found that aridity index (AI) and well depth were the strongest predictors of aquifer type. For dry regions (AI $>$ 1.48), wells at depths less than 241 meters are usually unconfined, while wells at depths greater than 241 meters are usually placed in confined aquifers. In more wet regions (AI $<$ 1.48), wells at depths less than 19 meters are usually in unconfined aquifers, while greater than 19 meters usually indicate a confined region. The cross-validation metric showed that this simple yet interpretable model could identify unconfined real observations of WTD with over 85% accuracy, while the overall accuracy in identifying the class of real observation (confined versus unconfined) was over 73%. This model was applied to the entire study region to label real WTD observations (and their corresponding wells) as confined versus unconfined. Finally, we excluded all observations labelled as confined. In the end, this led to 541,418 pixels (at 500 m resolution) of real observations of WTD. Other criteria for aggregating point-scale to pixel-scale observations can be found in Section 2.2.

3.2 Climate data resampling

This study aimed to estimate water table depths at a resolution of 15 arcseconds (500 m at the equator). However, the continental-scale climatic input variables explained in Section 2.1.1 were only available at coarser resolutions, such as 360 arcseconds. The coarse-resolution climate datasets in GIS raster formats were resampled to the 15-arcsecond target resolution using the Geographically Weighted Regression method (GWR). In this technique, the independent variable of the down-scaling was elevation. We used the GWR for Raster Down-scaling in the SAGA software package (Spatial and Geostatistics menu).

Table 1: Climatic, topographic, and soil characteristics of ten ecoregions along which we compare and evaluate the performance of our models. The characteristics include long-term average Aridity index (-) and Temperature ($°C$) as well as Elevation (m), Depth to Bedrock (DTB, cm), Shallow Clay (%), and real observation of WTD (m). Mean and median reflect the spatially averaged values of the characteristics across each ecoregion. The ten ecoregions are: Taiga (3), Northern Forests (5), Northwestern Forested Mtns (6), Marine West Coast Forests (7), Eastern Temperate Forests (8), Great Plains (9), North American Deserts (10), Mediterranean California (11), Temperate Sierras (13), Tropical Humid Forests (15). The location of these ten ecoregions are shown in Figure 2. Numbers in the parenthesis show the ecoregion class in the 15-class Omernik Ecoregion classification. Eco-region area is shown below the eco-region's class.

Region	Statistic	Aridity	Temperature	Elevation	DTB	Shallow Clay	WTD
(3)	Mean	0.75	-4.7	405	2331	17.1	4.12
$483km^2$	Median	0.74	-4.65	331	2382	18.1	2.47
(5)	Mean	0.78	1.22	404.97	2039	18.2	6.75
$48140km^2$	Median	0.76	0.98	370	1835	18.4	4.57
(6)	Mean	0.93	0.89	1366	1641	15.9	19.1
$27406km^2$	Median	0.73	0.51	1233	1525	15.7	8.60
(7)	Mean	0.26	3.53	605	1723	12.4	7.92
$21301km^2$	Median	0.21	3.47	406	1628	11.9	4.57
(8)	Mean	0.88	13.15	205	1705	20.3	5.31
$122212km^2$	Median	0.89	13.3	181	1453	21.0	3.96
(9)	Mean	2.26	10	684	3908	28.1	17.0
$228570km^2$	Median	2.16	8.88	616	3755	28.3	9.14
(10)	Mean	6.44	13.4	1320	3659	19.5	27.7
$76231km^2$	Median	5.13	12.0	1398	2376	19.7	15.0
(11)	Mean	3.86	16.1	433.2	1282	21.6	19.6
$16278km^2$	Median	3.42	16.3	283	801	21.9	14.3
(13)	Mean	2.31	14.9	1935	529	23.7	40.7
$2858km^2$	Median	2.01	14.5	2019	188	23.1	17.9
(15)	Mean	1.14	25.1	98.0	361	35.0	1.46
$857km^2$	Median	1.16	25.4	29	248	36.8	1.19

3.3 Machine learning modeling of WTD

3.3.1 Machine learning algorithm: XGBoost

Decision trees can be simple yet powerful and interpretable models of complex data. Methods that combine a large number of decision trees into an ensemble of trees could exhibit strong predictive capabilities and computational efficiency on tabular data (Shwartz-Ziv & Armon, 2022). Tree-based ensemble methods include random forests (Breiman, 2001) and gradient-boosted decision trees such as XGBoost (T. Chen & Guestrin, 2016), CatBoost (Prokhorenkova et al., 2018), and LightGBM (Ke et al., 2017). While random forests is the most popular tree-based ensemble method in hydrology (Tyralis et al., 2019), our preliminary results showed a stronger performance of XGBoost on our dataset. Other studies also showed the strong performance of XGBoost in the simulation of groundwater systems (Osman et al., 2021). XGBoost, the machine learning algorithm used in our paper to simulate WTD, is centred around the sequential optimization of shallow decision trees (James et al., 2013). A single shallow decision tree is a *weak* learner as it captures the broad relationships in the data with a minimal chance of overfitting. The sequential nature of the algorithm allows XGBoost to learn slowly while correcting itself during the learning process. This is captured by iteratively regressing the residuals of the previously built set of shallow trees. The learning rate and level of stochasticity can be controlled via various hyperparameters.

Building an XGBoost algorithm requires robust calibration and validation of regular XGBoost parameters and optimization of hyperparameters (Probst et al., 2019; Bilolikar et al., 2023). In developing each model setup, the (real and proxy) WTD observations are split into a training, validation, and test set. The regular XGBoost parameters are calibrated using the training set, and hyperparameters are calibrated against the validation set. In our study, the training set includes 1/3 (randomly selected) of the real and proxy observations within the R. M. Maxwell and Condon (2016) domain (Figure 3f shows this domain) and 2/3 of the (real and proxy) observations from the rest of study region. The validation set includes 1/3 of the (real and proxy) observations within the R. M. Maxwell and Condon (2016) domain + 1/3 of observations from the rest of the study region. The test set includes the remaining 1/3 of observations within the R. M. Maxwell and Condon (2016) domain. Such a split ensures that we fairly compare the simulations of R. M. Maxwell and Condon (2016) with our machine learning simulations and two other physically-based simulations, while training and validating evenly against the rest of the domain. 20 iterations of random search were used to select hyperparameters based on the model's performance (R^2) on the validation set. Once hyperparameters are chosen, the model is retrained on both the training and validation sets and tested on the test set. We report the performance of the three machine learning models against (real and proxy) WTD observations of the test set. The final simulation of each machine learning model is then made based on the full model trained on all data.

3.3.2 Implementing physical constraints

Domain knowledge can improve the generalization and extrapolation capabilities of machine learning models (Janssen & Ameli, 2021). In machine learning models, one way to add domain knowledge is to constrain the model via physically meaningful monotonic relations among input variables and the response (Fallah Tehrani et al., 2012; Ben-David et al., 2009; Bartley et al., 2019; Cano et al., 2019). A monotone increasing (decreasing) relationship between a variable x_j and the response y is defined as follows: given an increase in x_j, and that all other variables are held constant, the response should not decrease (increase) in value (Bartley et al., 2019; Fallah Tehrani et al., 2012). Utilizing monotonic constraints can decrease the size of the search space of *good* models, ensure sensible model behavior, increase generalizability, and improve comprehensibility (Gutiérrez & García, 2016; Bartley et al., 2019; Cano et al., 2019). While monotonicity is a strong assumption, it is clearly applicable across many areas of science (Liu et al., 2020). One prominent example of this, as suggested by Fallah Tehrani et al. (2012), is that doctors would not trust a model where increased tobacco consumption leads to a predicted decrease in lung cancer risk. Likewise, groundwater hydrologists should not trust a model in which increased precipitation, while keeping all other variables constant, leads to increased WTD predictions. XGBoost can easily incorporate such physically meaningful monotonic constraints (Dong et al., 2022; Bartley et al., 2019; Ovchinnik et al., 2019; Yang & Chui, 2021). Any split that violates the direction of monotonicity is rejected (Dong et al., 2022). Further, the mean values of a split are passed down to its children such that monotonicity cannot be violated further down in the tree (Dong et al., 2022; Bartley et al., 2019). This simple framework allows for guaranteed global monotonicity while not dramatically increasing computational cost (Bartley et al., 2019; Ovchinnik et al., 2019).

We imposed the following constraints to all three set-ups of machine learning models developed in our paper: (1) WTD must monotonically increase with a larger aridity index, and with larger deep/shallow sand fractions, and (2) WTD must monotonically decrease with precipitation, precipitation excess, deep/shallow clay fractions, and topographic index. Note that all other variables are left unconstrained. The location of the water table is a function of net groundwater recharge and how fast the system retains or laterally drains groundwater (R. Maxwell et al., 2015). The dominant processes controlling recharge include precipitation and evapotranspiration or aridity (Moeck et al., 2020). Indeed, we know from the simple mass-balance equation that spatial increases in long-term average precipitation and decreases in evapotranspiration, all else being equal, cannot lead to a decrease in groundwater storage. Similarly, a larger topographic index at a given pixel, all else being equal, implies a larger discharge of flow toward the pixel and should not be associated with deeper WTD. A larger sand fraction, all else being equal, may also suggest faster vertical/lateral drainage of groundwater, leading to deeper WTD. Conversely, a larger clay fraction may suggest a slower groundwater drainage, leading to shallower WTD. During our initial experimentation, we found that the model fit and test set R^2 decreased slightly due to adding constraints. Similar observations were seen in Ben-David et al. (2009) and Bartley et al. (2019). This may occur be-

cause the noise and biases available in our observational data may not obey monotonic constraints (Ben-David et al., 2009).

3.3.3 Three machine learning model setups

Three different sets of (real and proxy) observations of WTD were used to optimize XGBoost's (hyper)parameters, leading to the development of three machine learning model setups and WTD simulations. In the first model setup (V1), we only used 541,418 pixels of real observations of WTD from unconfined aquifers, with each real observation receiving a weight equal to 1. As we will see in the results section, this model could accurately simulate WTD along the observational locations while missing excessively shallow WTD close to permanent surface water bodies. Hence, we introduced the second model setup (V2), in which 12,167,332 pixels of WTD proxy data along the semi-permanently wet shorelines of surface water bodies were added to the real observations of WTD, in order to optimize the (hyper)parameters of the XGBoost algorithm. WTD was assumed to be zero at these pixels. These WTD proxy data received a weight equal to the magnitude of water occurrence probability (WOP) at the given pixel, which should be larger than 75%. Indeed, more persistent water inundations are more likely to have a zero WTD. See Section 2.3.1 for more details on delineating the semi-permanently wet shorelines of surface water bodies and the quantification of WOP.

As we will see in the results section, despite very accurate performance of V2 along and close to (real and proxy) observational locations, V2 led to excessively shallow WTD along some high-elevation steep mountainous landscapes. This contradicts the findings of local-scale studies, which have consistently observed a deep WTD along high-elevation mountainous regions (Manning et al., 2013; Smerdon et al., 2009; Ofterdinger et al., 2014; Somers et al., 2019). Indeed, due to a lack of real and proxy observations along high-elevation steep mountainous landscapes, V2 may not properly *learn* groundwater processes occurring along these landscapes. Height above the nearest water body (HAND) was shown to approximate WTD (Koch et al., 2019; Nobre et al., 2011), especially in dry regions with mountainous topography (Gleeson et al., 2011; Desbarats et al., 2002). Hence, HAND values in the mountainous regions of North America may offer a fair approximation of WTD in these regions. Thus, we introduced the third model setup (V3), in which 2% of pixels, with HAND values larger than 30 meters (a total of 766,814 pixels), were randomly sampled and added to the (real and proxy) observations used in V2 (see Section 2.3.2 for more details on HAND data). Along these pixels, WTDs were assumed to be equal to HAND values. Note that the 30-meter threshold represents the third quartile of HAND values, corresponding to the steepest and highest lands across the study region. HAND data could be a more uncertain proxy of WTD than the wet shorelines of surface water bodies, thus, a smaller weight of 0.75 was used for HAND data in V3 model development and optimization.

3.3.4 Interpretation of machine learning models

The same climatic and physical input variables were used for the three model setups (input variables were explained in Section 2.1). To interpret what the machine learning algorithm learnt, we can quantify and rank the extent to which XGBoost relies on each input variable in each modelling setup. To achieve this, we computed each input variable's gain feature importance metric in each modelling setup. The split-level gain metric of a given input variable was computed as the gain in accuracy after each split belonging to the input variable. The split-level gains were then averaged across all splits in the ensemble of trees to form the final gain metric of each input variable in each modelling setup (T. Chen et al., 2019). Such a metric aims to reflect the structure that the machine learning model learnt during model development (or optimization) and can be used to infer the extent to which such structure follows available scientific literature relevant to WTD prediction.

3.4 Model evaluation criteria

We compared the performances of our three machine learning-based and the three physically-based simulations of WTD within individual ecoregions and across the entire study domain. The *unseen* data against which the models' performance is evaluated include (1) *unseen* real WTD observations (OBS) and (2) proxy data on the permanently wet interior pixels of surface water bodies (WB), wherein we ex-

pect WTD to be zero (see Section 2.3.1 for more details on the delineation of these pixels). For the three machine learning simulations, unseen real WTD observations along the entire study region include a third of the available data within Maxwell's domain, which were not used in model training and validation. Within each ecoregion, unseen real WTD observations were identified through 10-fold cross-validation. Proxy data from permanently wet interior pixels of surface water bodies were not used in model training and validation and are technically unseen for the three machine learning simulations. The three physically-based simulations, to some extent, rely on real observations of WTD and/or the location of surface water bodies to obtain more optimal model parameters (see Section 2.4). However, to be fair to these simulations, in our paper, we assume that all real observations and proxy observations (e.g., the interior pixels of surface water bodies) are unseen by these physically-based models. Hence, for physically-based simulations, all real and proxy WTD observations were considered unseen across the entire study region and each ecoregion.

At pixels where unseen real and proxy data are located, we computed the mean absolute error (MAE) between simulations and real observations of WTD (MAE-OBS) and along the interior pixels of water bodies wherein zero WTD is expected (MAE-WB). The authors of physically-based simulations of WTD usually argue that their simulations of WTD are biased replicas (and not accurate simulations) of the observed WTD, as physically-based models do not account for human intervention. Human intervention due to pumping could significantly bias the observations of WTD, hence, we also estimated the correlation between simulations and real observations of WTD (Corr-OBS) at unseen well locations, using all 6 different simulations. In doing so, we evaluated how much each model captures the spatial variability of WTD without punishing physically-based simulations for possible pumping biases. In addition to comparing the performances of machine learning and physically-based models against unseen real and proxy observations of WTD, we explored the pixel-by-pixel statistical association among the six models, across the study region, to quantify their similarity. We do this by computing the correlation between each pair of simulations and visualizing it as a correlation matrix.

4 Results

4.1 Description and comparison of the spatial patterns of WTD simulations

4.1.1 Three machine learning-based simulations of WTD

Overall, the three machine learning simulations consistently show shallower WTD on the eastern portion of the continent of North America than the western portion (Figures 3a to 3c). However, WTD simulations exhibit significant differences among the three machine learning model setups at regional and local scales. V1 could not reasonably predict WTD close to (and within) lakes and rivers, particularly along lakes in Canada's North and Prairie Pothole Region, where WTD was predicted to be around 10m. In contrast, V2 accurately predicts that WTD should be near zero close to (and within) lake and river locations. However, such a model setup leads to excessively shallow (less than 0.1 m) WTD along the large portion of Canada (with the exception of the Canadian Prairies, South-eastern Canada and central British Columbia), while V1 is more conservative with predictions of 1-5 m in such locations. Regardless, the overall spatial patterns in V1 and V2 are similar, and these two simulations are highly spatially correlated (0.78), while V3 has a negligible spatial correlation with two other model setups (0.11-0.16) (Figure 4).

One notable distinction across the three model setups occurs along the Canadian Rocky Mountains, where V2 shows very shallow groundwater simulations, while V3 estimates the depth to be deeper than 50m along high-elevation steep lands, and V1 predicts a WTD of up to 10m. Furthermore, across the Canadian Rocky Mountains, WTD is highly spatially variable in V3, following the large spatial variations in elevation and slope, while V1 and V2 predict fairly spatially uniform WTD. Unlike V1 and V2, V3 follows the general patterns and magnitudes of Fan and de Graaf's simulations across the Canadian Rocky Mountains. Similarly, across the USA's Appalachia, V3 clearly distinguishes between the Appalachian Mountains of the eastern USA and the rest of the eastern USA. While V1 (V2) shows a fairly uniform distribution of WTDs in this region with no clear spatial pattern, V3 follows the general patterns and magnitudes of Fan and de Graaf's simulations with highly locally variable WTD. Across the USA's Appalachia, V3's WTD is deep ($> 50m$) along steep, high-elevation landscapes, while the rest of the east-

ern coast has distinctly shallower WTDs at 0-10m. Another major distinction occurs in the large portions of Canada's North surrounding Hudson Bay. In V1, this region has WTDs ranging from 1 to 20 meters, similar to de Graaf's physical-based simulation, whereas V2 predicts almost the entire region to have around zero WTD. While V3 predicts a large portion of this region with nearly zero WTD, some local areas have medium to high WTDs. V3 in this region follows Fan's simulation in terms of the spatial pattern of WTD. Finally, all three machine learning model setups, in line with Fan and de Graaf's simulations, predict that the southwestern deserts of the USA have extremely deep water table depths ($>$ 70 m).

4.1.2 Three physically-based simulations of WTD

The three physically-based simulations, on average, predict deeper WTD across western North America, while WTD is predicted to be shallower in the eastern part of the continent (Figure 3). WTDs embrace significant spatial variation in all three simulations at the regional scale. However, the magnitudes and spatial patterns differ substantially from one study to another, possibly due to differences in spatial resolution, input data, or methodology. On closer inspection, we can observe that de Graaf's simulations show consistently deep ($> 40m$) WTD for most of North America. In this simulation, western North America and the Appalachian highlands have extremely deep ($> 50m$) WTD, while most of the rest of the eastern United States have middling WTDs (5m-50m). One exception is southern Florida, where large areas uniformly have shallow WTDs (0m-5m). The overall spatial patterns of de Graaf and Fan's simulations are similar, although Fan's simulation has much greater local-scale spatial variability. This weakens the spatial correlation between de Graaf and Fan's simulations (0.33) (Figure 4). Maxwell's simulation of WTD across a large portion of the USA exhibits a much narrower range (0-55m) than the previously mentioned physically-based simulations. Simulations of WTDs above 30m are only limited to mountainous areas in the western USA. Most of the eastern USA is predicted to have 1-10m WTD while most of Northern Minnesota, Wisconsin and Michigan have WTDs of less than 1 meter.

In terms of the magnitude of WTD at the regional scale, Fan's simulation, in line with V3, shows that the lower Mississippi River basin, the coastal region from southern Florida to New Jersey, the midwest United States, and northeastern Canadian wetlands have generally shallow WTDs ($< 5m$). At the same time, local areas of deep WTDs also exist along mountainous ridges of the Rockies and Appalachia for both Fan and V3 simulations. Generally, Fan and V3 exhibit high local variability, which arose from simulating the phreatic surface as a flat surface at the local scale, particularly in mountainous regions (i.e., British Columbia). This leads to shallow WTD$<$ 5m in the valleys between mountain peaks and deep WTD$>$ 100m on the mountain ridges. Indeed, WTD strongly follows local-scale elevational differences in both Fan and V3 simulations.

4.1.3 Statistical associations among six machine learning and physically-based simulations of WTD

Analysis of pixel-by-pixel spatial correlation between each pair of WTD simulations, using all pixels of the study region, depicts there is generally a weak spatial correlation among the three physically-based simulations of WTD ($0 < r < 0.33$) across the USA and Canada (Figure 4). There is also a weak spatial correlation between the three physically-based simulations of WTD and the V1 and V2 setups of machine learning-based simulations ($0.11 < r < 0.38$). Interestingly, while the three physically-based WTD simulations are almost uncorrelated, they are correlated ($0.52 < r < 0.62$) with our V3 model setup. V1 and V2 are highly correlated with each other ($r = 0.78$), but are less correlated with V3 ($r = 0.16, 0.11$). Such quantified correlations support the continental-scale spatial distribution of simulated WTDs shown in Figure 3 and the corresponding comparisons made in the previous subsections.

4.2 Interpretation of Three Machine Learning Models

This section interprets the importance of the input variables within each of our three machine learning model setups (Figure 5). V1 strongly relies on climatic features such as temperature and aridity index to explain the variability of real observations of WTD, with both being responsible for over 10% of the model performance. In total, climatic features have a part in over 60% of V1's performance, and to-

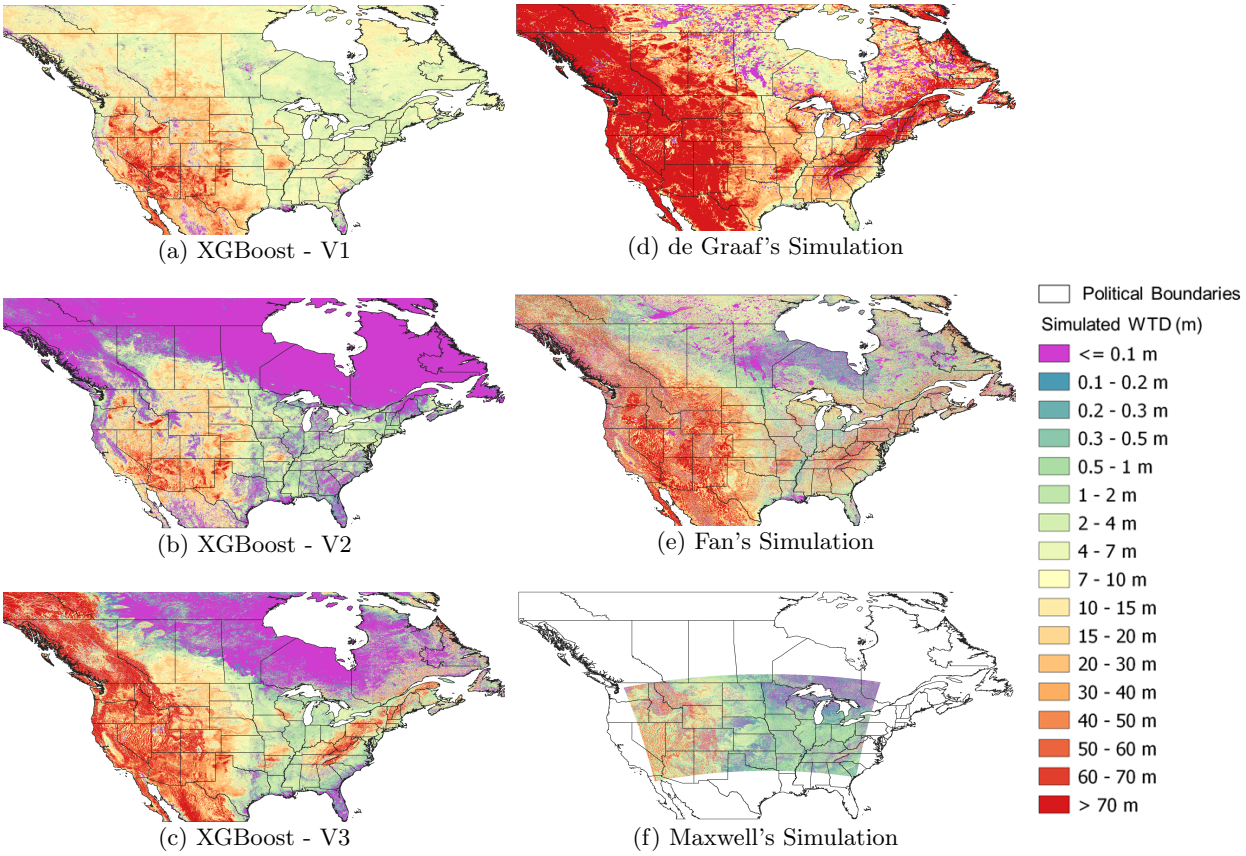

Figure 3: Six different simulations of water table depths across the US and Canada using machine learning models (a-c) and physically-based models (d-f).

pographic features explain more than 25%, with close to 15% of the impact coming from elevation. Landcover and soil properties make up the rest of the model. While landcover and sand (and clay) related fractions contribute the least ($< 5\%$), shallow and deep silt fractions and depth to bedrock play moderately strong roles ($5-10\%$). In V2, the aridity index greatly impacts model performance ($> 10\%$), while almost all other climatic, topographic and soil-related properties have uniformly moderate ($5-10\%$) effects on V2 model performance.

V3 is almost exclusively reliant on topographic variables ($\approx 70\%$ in total), such as topographic index ($\approx$ 37%), slope ($\approx$ 15%), and elevation ($\approx$ 17%). In total, climatic features explain only 15% of the model, with January temperature having the largest impact ($\approx 5\%$), while V3 has little (less than 5%) reliance on snow fraction, precipitation, precipitation excess, maximum snow water equivalent on the ground, and rainfall intensity. V3 only slightly relies on sand/silt/clay fractions (less than 5%), while it is moderately reliant on depth to bedrock ($\approx 5\%$) (Figure 5).

Overall, V1 and V2 rely on topographic variables (topographic index, slope, and elevation) at about the same level, while V3 is over twice as dependent on these variables. V1 (V3) is strongly (weakly) reliant on climatic information, while V2 gives almost all input variables a more or less uniform score (Figure 5). Land cover does not seem to be a useful variable across all models. Soil-related features such as sand and clay fractions are only given relatively high importance by V2. The stark differences in simulating WTD in mountainous areas between V1 (or V2) and V3, as explained in Section 4.1.1, likely have to do with V3 being strongly driven by local topography instead of climate, while V1 (or V2) is strongly driven by climate. Note that the variable importance metric used in this study is only meant to inter-

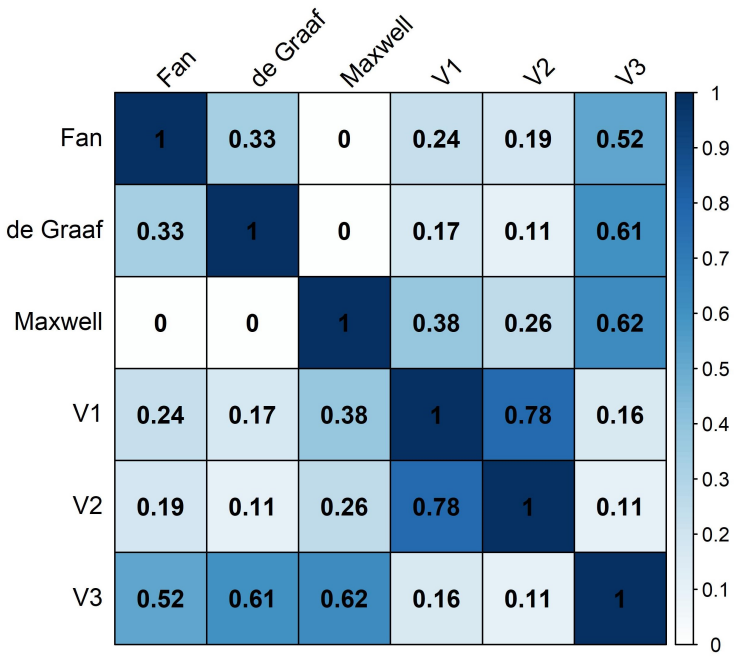

Figure 4: Pixel-by-pixel spatial correlations among six different physically-based and machine learning WTD simulations.

pret each model, not the underlying physical processes. Thus, from this analysis, we can only conclude how heavily each model uses each variable to explain the variability of target observations, not how strongly each variable is related to WTD in general (see Janssen et al. (2023) for details). This important dichotomy is illustrated by the fact that each model gives vastly different importance scores and the ground-truth importance scores are currently unknown. Further, it is important to note that these importance scores are only related to the spatial heterogeneity of WTD, and it does not consider temporal variation.

4.3 Comparison of Six Models' Performances in Simulating WTD at Unseen Locations

This section compares each model's ability to predict WTD at pixels wherein unseen real and proxy observations are located within each ecoregion and throughout the study region. Mean absolute error (MAE) and Pearson correlation were used as performance metrics to evaluate model performance in predicting observed or expected WTDs at unseen locations. A summary of predictive performance results for each ecoregion and the entire study region can be found in Table 2.

Along the Temperate Sierras (13), MAE-WB values are highest, meaning all six models perform poorly (MAE-WB > 2) in predicting permanent water body locations. This ecoregion exhibits the largest elevation across the study region (median of 2019 m). All models, except V2, perform poorly in predicting permanent water bodies along the North American Desert (10), which has the highest aridity among all ecoregions and the second-highest elevation. Again, all models, except V2, perform poorly in predicting permanent water bodies in Mediterranean California (11), which has the second highest aridity. In the Eastern Temperate Forest (8), with the second lowest average elevation, V2 and V3 perform exceptionally well (MAE-WB≈ 0.1), and Fan (MAE-WB≈ 0.3) and Maxwell (MAE-WB≈ 0.7) perform very well, in predicting small water bodies. In the Great Plains (9) and Northern Forest (5) ecoregions, V2 and V3 perform exceptionally well and Fan performs very well. Along the Northwestern Forested Mountains (6) and Marine West Coast Forest (7), V2 is the only simulation with a strong performance in predicting permanent water bodies (MAE-WB$\approx$ 0.1). Unsurprisingly, the region with the lowest average observed WTD (i.e. the tropical humid forests of Florida (15)) also has the lowest error in locating per-

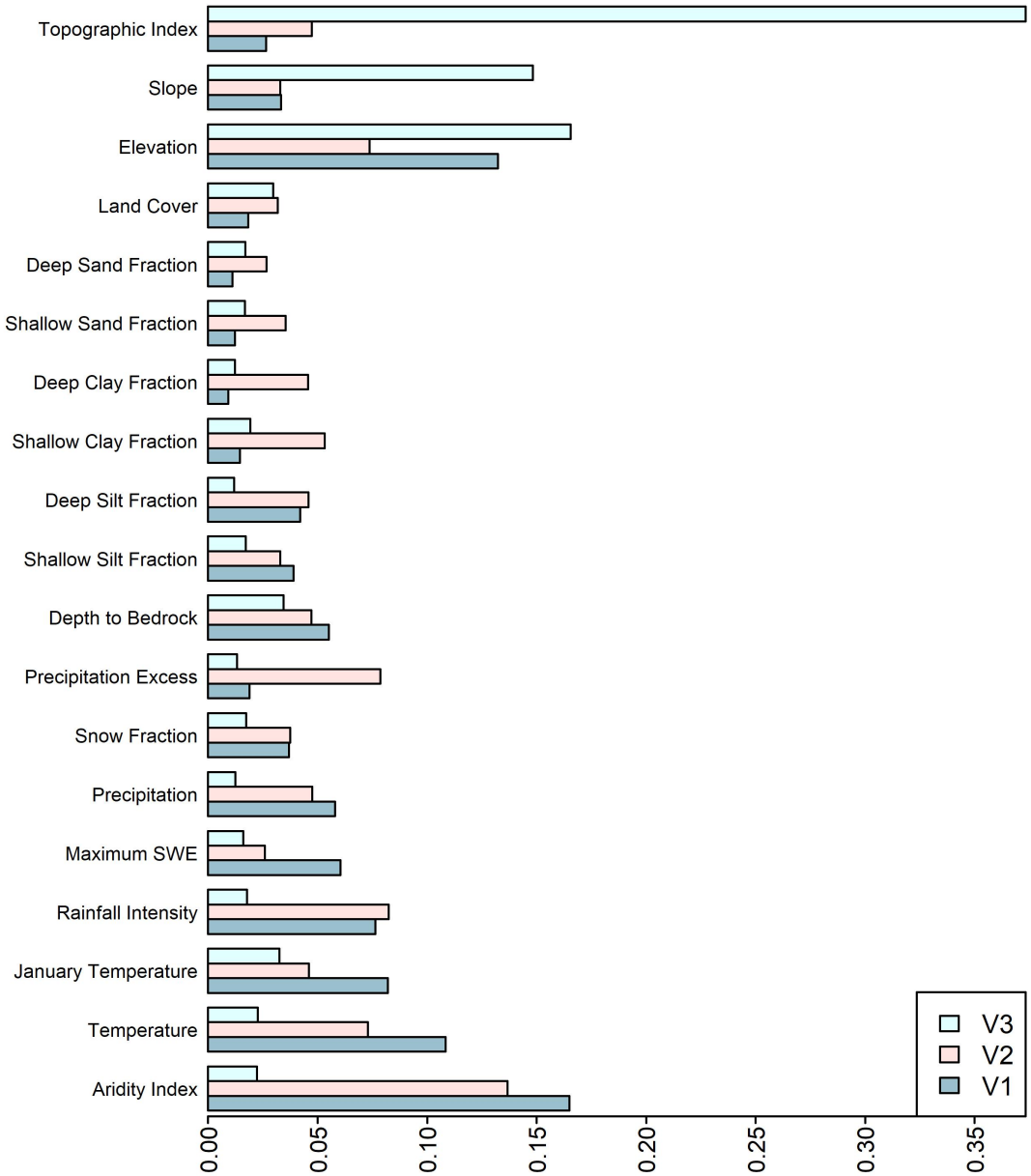

Figure 5: Relative importance of each input variable within each machine learning model setup (see Section 3.3.4 for the details on the derivation of importance score). The importance scores across a single model setup add to one.

manent water bodies across all models, with V2 and V3 performing exceptionally well (MAE-WB ≈ 0). Throughout the entire study region, V2 (MAE-WB=0.1) simulation best predicts the unseen interior locations of permanently wet surface water bodies. V3 (MAE-WB=2.42) and Fan (MAE-WB=2.54) simulations also perform fairly well, while V1 (MAE-WB=5.38) and de Graaf (MAE-WB=15.36) simulations are quite poor in this respect. Maxwell accurately simulates the unseen interior locations of permanently wet surface water bodies along their model domain, which covers a large portion of the USA (MAE-WB=0.94).

Table 2: The performance of each model on predicting "unseen" real observations of water table depth (OBS) and unseen interior pixels of permanently wet water bodies (WB) across the entire study area (All) and within each ecoregion. The performance is evaluated using (1) (MAE-WB) Mean absolute Error of simulated WTD at interior locations of permanently wet surface water bodies wherein zero WTD is expected, (2) (MAE-OBS) Mean absolute Error of simulated versus observed WTD, and (3) (Corr-OBS) the correlation between simulated and observed WTD. Ecoregions include: Taiga (3), Northern Forests (5), Northwestern Forested Mtns (6), Marine West Coast Forests (7), Eastern Temperate Forests (8), Great Plains (9), North American Deserts (10), Mediterranean California (11), Temperate Sierras (13), Tropical Humid Forests (15).

Region	Real Obs	Eval	Fan	de Graaf	Maxwell	V1	V2	V3
(3)	483	MAE-WB	2.53	49.23	NA	5.58	0.04	2.83
		MAE-OBS	3.93	29.19	NA	7.38	6.69	28.71
		Corr-OBS	0.18	0.31	NA	0.50	0.43	0.05
(5)	48140	MAE-WB	0.91	17.07	0.92	3.90	0.06	0.32
		MAE-OBS	8.54	30.62	3.95	3.96	4.64	6.10
		Corr-OBS	0.03	0.09	-0.01	0.54	0.51	0.29
(6)	27406	MAE-WB	4.56	91.04	NA	6.62	0.09	5.52
		MAE-OBS	21.87	152.07	15.77	11.83	12.20	16.26
		Corr-OBS	0.18	-0.07	0.08	0.73	0.71	0.47
(7)	21301	MAE-WB	9.90	194.36	NA	5.09	0.10	11.97
		MAE-OBS	11.97	65.69	NA	5.02	5.02	6.95
		Corr-OBS	0.13	0.05	NA	0.60	0.60	0.38
(8)	122212	MAE-WB	0.30	3.66	0.71	3.04	0.10	0.10
		MAE-OBS	7.16	23.02	5.49	2.73	3.25	4.22
		Corr-OBS	0.18	0.09	0.04	0.62	0.52	0.28
(9)	228570	MAE-WB	0.79	15.24	1.39	4.96	0.12	0.38
		MAE-OBS	13.33	39.20	16.08	8.62	8.47	9.22
		Corr-OBS	0.38	0.20	0.04	0.70	0.69	0.64
(10)	76231	MAE-WB	8.12	139.18	3.92	9.30	0.53	4.67
		MAE-OBS	23.36	94.55	25.69	14.28	15.32	17.25
		Corr-OBS	0.37	0.14	0.11	0.73	0.69	0.55
(11)	16278	MAE-WB	7.76	116.09	NA	9.55	0.65	4.57
		MAE-OBS	14.74	72.41	NA	9.10	8.68	12.14
		Corr-OBS	0.24	0.08	NA	0.72	0.71	0.49
(13)	2858	MAE-WB	9.96	202.93	2.96	22.33	2.19	9.70
		MAE-OBS	39.20	479.42	39.21	29.21	29.21	29.76
		Corr-OBS	0.10	-0.02	0.03	0.57	0.57	0.19
(15)	857	MAE-WB	0.29	1.93	NA	1.67	0.05	0.03
		MAE-OBS	1.46	1.36	NA	0.96	1.31	1.31
		Corr-OBS	0.09	0.10	NA	0.12	0.26	0.09
All	541418	MAE-WB	2.54	40.78	0.94	5.38	0.10	2.42
		MAE-OBS	13.47	52.90	15.36	7.81	8.18	9.61
		Corr-OBS	0.40	0.21	0.09	0.75	0.71	0.60

Overall, the machine learning-based simulations predict the unseen real observations of WTD across the entire study region (Corr-OBS between 0.6-0.75) stronger than physically-based simulations (Corr-Obs between 0.09-0.4). Within ecoregions, both MAE and correlation metrics depict that all three machine learning-based simulations perform stronger in predicting unseen real observations of WTD, except in Taiga (3), where Fan simulations perform better than V1 and V3 on a small number of observations.

In predicting WTD at unseen wells across the entire study region, V1 performs the best among all models with a correlation of 0.75 and MAE of 7.81. This is not surprising since it is the only simulation exclusively driven by real observations of WTD. Although most of V2's training data comes from proxy observations (and not real observations of WTD), its performance on predicting unseen real observations degrades very little, with a correlation of 0.71 and an MAE of 8.18. The errors and accuracies among these two models and within each ecoregion also correspond closely. V3, generally, performs worst among the three machine learning models in predicting real observation of water table depth while still performing better than physically-based models.

5 Discussion

This paper presented three physically constrained machine learning (XGBoost) simulations of WTD. The three models (V1, V2, and V3) were built by sequentially adding proxy observations relevant to WTD (see Section 3.3.3). Unseen real and proxy observations of WTD, which were not used for training and validation of machine learning models, were then employed to explore and compare the performances of the three machine learning simulations and three available physically-based simulations of WTD across ten ecoregions of North America. Overall, all six models poorly predict WTD across three ecoregions with the highest aridity and elevation (Temperate Sierras, North American Desert, Mediterranean California). In the rest of the USA and Canada, along locations with available real and proxy observations of WTD, V1, V2, and V3 perform well while physically-based models fail to accurately follow the variability or magnitudes of well-based observations. The interpretation of the three machine learning models suggested that the V3 model strongly used the topographic wetness index (TWI) information to simulate WTD, while V1 strongly relies on climatic information. In this regard, V1 resembles Ma et al. (2024)'s machine learning simulations of US WTD, which used random forests trained on only well-based observations of WTD.

One may argue that the information that V3 learnt from the data and used to predict WTD corroborates well with classical integrated groundwater-surface water models (e.g., TOPMODEL (K. J. Beven et al., 2021)), in which TWI dominantly controls the spatial pattern of WTD. Recent hillslope-scale experimental works in both wet and arid mountainous landscapes also suggested that TWI dominantly controls the location of WTD from the hillslope ridge line (where TWI is small and WTD is deep) to the hillslope toe (where TWI is relatively large and WTD is shallow) (e.g., van Meerveld (2024); Karlstrom et al. (2023)). Among the three machine learning simulations, V3 not only somewhat strongly follows WTD observations in most of North America's ecoregions, it also generates predictions which are highly spatially correlated with simulations from Fan's and de Graaf's physically-based models, particularly along mountainous regions. Indeed, V3 provides a good balance between what (real and proxy) data dictates and what physically-based models suggest. However, both data and model structures, including the structures of physically-based and machine learning models, are uncertain and difficult to verify. These uncertainties will be critically discussed below. Hopefully, such a critical discussion will guide future works on data collection and compilation as well as model development and verification in groundwater hydrology.

5.1 Uncertainty in the observations of WTD

To assess the reliability of different WTD simulations, we must rely on historical observations of well-based water levels. However, these real observations may have associated errors and, under some circumstances, may not represent the water table depth meaningfully. This is particularly important as the model evaluation statistics can depend strongly on the sample of observations on which one chooses to evaluate the model (see Reinecke et al. (2020) and Table 2). In the remainder of this subsection, we explore uncertainties related to the real observations of WTD and how they can affect the simulations of WTD and the verifiability of those simulations.

Observations of WTD are susceptible to systematic errors due to vertical hydraulic gradients (Jasechko & Perrone, 2020). It is fairly well known that water tapped within confining layers can experience additional pressure heads, leading to extremely shallow measurements of well water levels. In these systems, the vertical gradient would be upwards, and the true water table would be far deeper than what the read-

ings from well observations convey (Vincent et al., 2013; Hilton & Jasechko, 2023). Very few well observations have indicators (and labels) of whether or not a confined or unconfined aquifer is tapped, further adding to the uncertainty of observations of WTD. The upward vertical gradient issue can even arise in unconfined aquifers, especially in the valley bottoms of steep terrains (Hilton & Jasechko, 2023). Furthermore, downward hydraulic gradients could be common in some landscapes (Elçi et al., 2003; Jasechko & Perrone, 2020; Gabrielli et al., 2018), where the WTD could be measured far below the true water table. This can happen due to fairly independent causes such as long well screens (Elçi et al., 2003). Theoretical and numerical simulations conducted by Elçi et al. (2003), as well as an experimental study conducted in California by Jasechko and Perrone (2020) depicted this phenomenon. Indeed, well levels are only a good representation of the water table when the well screen is placed at (or close to) the true water table or where perfectly hydrostatic conditions exist (Vincent et al., 2013; Jasechko & Perrone, 2020).

Although the 500 m resolution used in our study represents the finest-scale available for simulations of WTD on the North American continent, generating gridded observations from point-scale observations of WTD (as explained in Section 2.2) could also create data uncertainty (Gleeson et al., 2021; Reinecke et al., 2020; Klemes et al., 1982). At a 500 m^2 pixel, WTD can still be spatially variable and diverge from the pixel-scale average computed from the point-scale observations of the pixel. This is particularly true where the pixel covers diverse landscapes, including steep hillslope, hillslope toe, and riparian area wherein point-scale observations of WTD can significantly diverge from the pixel-average WTD (de Graaf et al., 2017; Gleeson et al., 2021; de Graaf et al., 2015). This issue could also be relevant to the proxy observations (or shorelines of water bodies), where the difference in WTD (and the probability of inundation occurrence) within a 500 m pixel could be vast.

Human error could also cause some types of data uncertainty. Across our study region, several real WTD observations are unreliable, such as over 100 USGS observations showing a water level deeper than the deepest well ever drilled in North America and thousands of USGS observations showing negative WTDs. Various other obvious errors have been detected in other works as well (Jasechko & Perrone, 2020). While these detected observations are wrong and should be removed before training or validating a model (as was done in our paper), other observations may be equally wrong, but impossible to detect and remove. In addition to large human errors, which may be present in a minority of observations, random observational errors can occur everywhere (Vincent et al., 2013). For example, Silliman and Mantz (2000) found that noise in water level measurements is high enough to prevent the estimation of the vertical hydraulic gradient.

Pumping has greatly affected groundwater levels across the US, especially in the last hundred years (Hilton & Jasechko, 2023). Groundwater pumping can have an outsized impact on lowering the water table in warm, low-elevation landscapes due to the higher likelihood of agricultural uses (Fan et al., 2013; Gleeson et al., 2021). Pumping can affect WTD observations near and in the surrounding areas where pumping occurs. Under this condition, the observations collected near and in the surrounding pumping areas would not necessarily reflect the WTD (Jasechko & Perrone, 2020). With data from California, Jasechko and Perrone (2020) found that pumping could cause temporary drawdowns of 10s of meters. Even after the use of a well has ceased, an artesian well may continue to extract groundwater and affect observations of WTD (Hilton & Jasechko, 2023).

Temporal variability of the water table may hinder our ability to identify static WTD at a particular location (Molénat et al., 2005). A large portion of real observations in the USA and Canada ($\sim 81\%$) were taken at one time, with no follow-up observations at that location. Water levels can fluctuate due to long-term or oscillatory changes in climate, tides, runoff, barometric pressure, mass loading, or pumping (Condon et al., 2021; Rust et al., 2019; Rasmussen & Crawford, 1997; Flickinger & Mitchell, 2020; Molénat et al., 2005; Hayashi et al., 2016; Jasechko et al., 2024). Appraisal of USGS data depict, for example, in a well near Seco Creek, Texas, the WTD fluctuated by over 50 meters in less than two decades of observations. For a USGS groundwater well in San Bernardino, California, yearly oscillations occur with an amplitude of nearly 10 meters, with an additional decreasing trend from about 30 meters in 2005 to 60 meters in 2020. Such temporal variation of WTD could also happen in regions with typically shallow WTD, such as the prairie pothole region of central USA and Canada. In this region, the water table may fluctuate by over 6 meters in less than a decade, even without pumping influences, as exemplified by Hayashi et al. (2016). In aquifers worldwide, long-term trends of 10 m to over 100m in observed

WTD can be caused by excessive pumping (Jasechko et al., 2024; Lopes et al., 2006). Even when we exclude pumping effects, natural seasonal variations were shown in Nevada to vary WTD by about 6m (Lopes et al., 2006).

Finally, and perhaps most importantly, large-scale sampling biases across the USA and Canada have affected the overall spatial pattern of available observations of WTD (Reinecke et al., 2023). Hydrologists and engineers typically dig wells where there is likely water (i.e., river valleys and productive aquifers). If a well is dug to some maximum acceptable depth and no water is found, no WTD measurement can be taken. Hence, deep WTD observations are not widely available across North America. Furthermore, the WTD observation dataset can be biased towards observations in low-elevation areas with large populations and moderate climates instead of dry (or wet) high-elevation areas (Boerman, 2022; Lopes et al., 2006). Therefore, the overall distribution of observations of WTD, available for modeling studies, may be shallower than the actual distribution of WTD across the USA and Canada (de Graaf et al., 2015).

5.2 Uncertainty in physically-based model structure and simulations

All three physically-based groundwater models analyzed in this work are based on similar governing equation. Fan et al. (2013) bases their model on the mass balance between recharge and lateral groundwater flow, where Darcy's law determines the latter. Darcy's law (and Richard's equation) was also the core governing equation of Parflow, developed by Kollet and Maxwell (2008). de Graaf et al. (2015) uses MODFLOW, which is also based on Darcy's law, to simulate groundwater and water table depth. The simulations of WTD, however, are wildly different across the three models (Figure 3). For example, Fan's simulation is more (locally) spatially heterogeneous compared to de Graaf, and Maxwell's WTDs are significantly shallower than those of de Graaf. Overall, the simulations of Maxwell share zero pixel-based spatial correlation with other physically-based models, while the correlation between Fan and de Graaf's simulations is quite low (Figure 4). These discrepancies point towards the fact that groundwater systems are chaotic systems. Indeed, the use of slightly different input data or boundary conditions while using a similar set of governing equations could lead to large distinctions in the simulations of WTD. The disparity in WTD simulations across different physically-based models shown in our paper further emphasizes the challenge of accurately representing the complexities of groundwater behavior at a large scale (e.g., global scale) (Gnann et al., 2023; Reinecke, Foglia, Mehl, Trautmann, et al., 2019).

The uncertainty in physically-based models' simulations is also revealed when we compare their simulations to observations. If the set of equations driving these models are based on physical laws and rely on reasonable assumptions, their converged solutions should closely match observations. However, this is not what we and others have observed. The correlation between observations and physically-based model simulations of WTD is small for Fan et al. (2013) (0.40), de Graaf et al. (2015) (0.21) and R. M. Maxwell and Condon (2016) (0.09). Looking at Table 2, we can see that the within ecoregion correlations are often even lower. Although the correlations are already quite low, they likely give us too much confidence in physically-based simulations since their R^2 (aka NSE) values are often negative (not shown in Table 2). These "abysmal" results are obfuscated in previous works, since model performance evaluation in the previous works was typically based on the comparisons between observed and simulated hydraulic heads instead of WTD (Reinecke et al., 2020). Such an evaluation cannot sufficiently evaluate the uncertainties of WTD simulations since almost all spatial variability of hydraulic head can be explained by the spatial variability of elevation. Indeed, as elevation is the major driver of both simulated and observed hydraulic head, obtaining R^2 close to 1 between observed and simulated hydraulic heads does not necessarily indicate strong model performance in WTD's simulation (Reinecke et al., 2020). For example, if WTD were predicted to be 5 m everywhere across North America, the R^2 between observed and simulated hydraulic heads would be above 0.99, while R^2 between observed and simulated WTD would be negative. There might be many reasons for the poor performance of physically-based models compared to real observations of WTD. This could be due to uncertain input data, numerical instability, incorrect (or missed) boundary conditions, poor parameter estimation, or the invalidity of Darcy's law at coarse spatial scales (Molénat et al., 2005; Gnann et al., 2023; K. Beven, 1989).

Studies on physically-based simulation of WTD related their poor model performance against real observations of WTD to data uncertainty of the observations caused by widespread pumping (Fan et al.,

2013; R. Maxwell et al., 2015; de Graaf et al., 2015). There are no reliable estimates of groundwater abstractions (and return flows) since irrigation pumpage, the largest groundwater use sector, is rarely systematically measured (Gleeson et al., 2021). Even if globally accurate datasets of groundwater abstractions existed, this may not significantly reduce simulation errors of physically-based models. For example, Reinecke et al. (2020) designed a theoretical study using the G3M model and found that the systematic underestimation in the simulation of WTD could not be resolved even if the pumping effect is accurately accounted for. This implies that other issues related to the model structure, in addition to the unknown pumping effect, could play significant roles. One of these issues could be the coarse spatial resolution of physically-based models that simulate WTD. However, Reinecke et al. (2020) suggested, based on the groundwater model developed for New Zealand, that increasing spatial resolution was not enough to resolve the large biases between observed and simulated WTD. They showed that most (incremental) improvements relevant to increasing spatial resolution could be caused by decreased within-pixel variability of real observations and not by improved model structure. Several researchers suggested that extending laboratory-scale equations to large-scale hydrological simulations is unjustified and has seen little-to-no success (K. Beven, 1987, 1989; Seibert, 2003). Indeed, integrating laboratory-scale physics to 100 m or 250 m scales is not theoretically justified (K. Beven, 1989), and these scales are not even reachable in large continental-scale physically-based groundwater models. Hydrologists should consider that large-scale applications of Darcy's law incur more than just approximation error since it can be argued that large-scale driving processes of groundwater systems may functionally differ from those indicated by laboratory-scale Darcy's law (Kirchner, 2006).

A lack of high-quality input data of important drivers of WTD could also prevent physically-based models from matching the observations and matching each other. Gnann et al. (2023) suggested that the uncertainties in the estimates of actual evapotranspiration and groundwater recharge could partially explain the mismatch between observed and simulated groundwater hydraulics. Koirala et al. (2014) noted that while higher resolution DEMs are available and could improve predictions, other important variables, such as climate and soil textures, are unavailable at the same resolution. Koirala et al. (2014) also noted that large differences between their WTD simulations and those of Fan et al. (2013) could be due to different groundwater recharge forcing datasets. Alongside climatic recharge and topography, hydraulic conductivity is arguably among the most important features for groundwater modelling, yet it is the most uncertain. There is also no clear path to resolving this issue since there is no way of directly measuring grid-scale hydraulic conductivity (K. Beven, 1993). While the lack of high-quality input data could also affect machine learning simulations, such an effect could be mitigated in machine learning models as they could automatically reduce the weight (or importance) of such uncertain data while the model is being optimized.

5.3 Uncertainty in machine learning-based simulations

The rapid adoption of machine learning within hydrology has led to several important advancements due to these algorithms' ability to easily model and predict hydrology's complex and non-linear processes. Yet, several shortcomings still remain for groundwater modelling using machine learning frameworks, as evidenced in our paper by the lack of fit among models as well as the lack of fit between simulations and observations of WTD. The three primary shortcomings are the overreliance on observational data, equifinality of model structure, and the inability to directly model physical processes (Istalkar et al., 2023; K. Beven, 2002).

The three machine learning-based groundwater models analyzed in our work are based on the same powerful machine learning algorithm, XGBoost, and the same set of physically-based constraints. Yet each model provides locally distinct simulations of WTD (Figure 3). Furthermore, the model performance against unseen real observations of WTD is not strong. Using similar tree-based machine learning methods, Koch et al. (2019) and Koch et al. (2021) found that the highest R^2 against unseen observations they could achieve across Denmark was about 0.55. Further, Ma et al. (2024) showed that random forests, could obtain 0.65 test set NSE with respect to log-transformed WTD along the large portion of the USA (same domain as R. M. Maxwell and Condon (2016) in Figure 3f). Our test set R^2 (NSE) against unseen real observations of WTD across the USA and Canada was quite similar at 0.56 for V1, and going as low as

0.35 for V3. Within individual ecoregions, the R^2 against unseen real observations of WTD was always slightly lower than the score on all of North America.

Typically, stronger performance against observational data is preferred, and systematic biases and large random errors in predictions could suggest that the developed model misinterpreted the groundwater system's physical laws. However, due to the considerable uncertainties of the observational data (see Section 5.1), it is unclear if the models that make the best predictions against real observations of WTD (V1 and V2) are truly the best. Experimental and modeling studies revealed WTD is usually extremely deep across steep (and wet) portions of the Rocky Mountains of Canada, in line with the simulations made by V3 (J. Chen et al., 2020; Fan et al., 2013; de Graaf et al., 2015; Smerdon et al., 2009). Yet in the corresponding ecoregions (6 and 7), the performance of V3 is worse than V1 and V2 (but still better than the physically-based simulations), if one considers the real observations of WTD as ground truth (Table 2). Without well-regulated observations that reflect the true WTD, we, as groundwater hydrologists, will forever be blind to the ground truth. With many parameterization (or model structure) options available with machine learning algorithms, only reliable observations can help us choose the correct path. If we knew the exact physical equations driving water table location at a coarse scale (e.g., 500 m) and could engineer a model that perfectly follows these equations, the reliance on training observational data would be less, and one could ignore biased training data. But clearly, these coarse-scale ground-truth equations have yet to be found (Section 5.2).

Equifinality can have a profound negative effect on the trustworthiness of machine learning simulations. During hyperparameter tuning and training, we noticed that there are likely many XGBoost parameter sets spanning wide ranges of the parameter and hyperparameter space, with satisfactory performance on the validation/test set. Indeed, as other studies showed, the most complex and least interpretable models often have the best predictive capability (Nearing et al., 2021; Yang & Chui, 2021). To manage equifinality, one solution is to add physical realism by adding physical constraints to machine learning algorithms, as we did in our paper. However, this practice reduced our models' predictive capability, as noted at the beginning of this section and as shown in other studies as well (Yang & Chui, 2021). One possible explanation is that adding physical realism to part of a machine learning model, in the form of monotonically constraining relationships of some variables, could diminish the physical realism of other more uncertain parts of the model as exemplified in Yang and Chui (2021). To properly constrain machine learning models, a better understanding of all physical relationships among inputs and output data and/or more diverse observations relevant to different processes connecting the input to output is needed (K. Beven, 2002).

Machine learning models can far "outperform" physically-based models on test set data (as shown in our paper and other studies, e.g., Nearing et al. (2021)). However, given the high sampling biases of our real observations of WTD (see Section 5.1), machine learning is still not guaranteed to "physically outperform" physically-based models across unmeasured or unmeasurable locations. Although we attempted to enhance the physical realism of our machine learning models through the use of additional proxy observations and physics-based constraints, we still expect future works could further enhance the physical realism of machine learning models in groundwater hydrology. We will discuss these points further in the next section.

5.4 Future opportunities to improve large-scale simulations of WTD

Currently, our knowledge about water table locations is highly uncertain and stored in hearsay and newspaper reports (Jasechko & Perrone, 2020). This is mainly because potentially uncertain and equifinal physically-based or machine learning model structures cannot be verified with potentially uncertain (and non-representative) observations of WTD. Here, we discuss future directions for improving the physical realism and verifiability of models in groundwater hydrology, with a particular emphasis on machine learning models.

The physical realism of machine learning models could be enhanced by incorporating known groundwater hydrology physical laws (e.g., Darcy's Law). However, there is no guarantee that including these laws would *verifiably* increase the physical realism of models at the scale of interest. This is also true for the physically-based models where laboratory-scale physical laws may not control pixel-scale groundwa-

ter processes. How climate, topography, and geology interact at local and regional scales could have an outsized effect on the pixel-scale WTD. Indeed, groundwater flow is not only driven by the landscape attributes at a given location but also by that of surrounding areas (Grabs et al., 2009). For example, snow processes, such as blowing snow and runoff over the frozen ground, may have pronounced causal effects on groundwater levels several kilometres away (Hayashi et al., 2016). Yet, such complex and spatially-varying interactions and the functional relationships connecting landscape attributes (locally and regionally) to WTD are unknown and understudied. Once such interactions and functional relationships are defined, they could be used to select among many candidate models or incorporated a priori in machine learning models.

Reliable verification among competing machine learning models could be made possible by testing how competing groundwater models simulate known causal relationships between the drivers of WTD (e.g., precipitation, topographic index) and WTD (or hydraulic gradient). This can be done using metamorphic testing if we know a priori the function and form of causal relationships among the drivers and WTD (Yang & Chui, 2021). The linear physical constraints used in our paper (see Section 3.3.2) are a simple form of such causal relationships. However, in reality, the functional forms of such relationships at local and regional scales can be more complex than what we used in our paper. Hence, future experimental or statistical inference studies could focus on exploring the functional form of such causal relationships at different scales. Another alternative to verify models could be the use of virtual experimentation wherein the competing machine learning models virtually simulate land use and climate alterations to choose which model more reliably replicates known behaviour (Kirchner, 2006).

The process-oriented indices, data, and markers with information relevant to WTD can improve machine learning-based groundwater models through different pathways. They can be used as (1) input variables to the model, as done for the topographic index in our paper, (2) proxy observations for model training, as done for the HAND and the probability of surface inundation in our paper, (3) model constraints or boundary conditions, or (4) as an (in)direct verifier of the model findings to differentiate between models that make good predictions for the right reasons versus those that make good predictions for the wrong reasons. For example, previous works showed that the incorporation of information on the landscape's hydrologic functioning (i.e. how landscapes store and transmit groundwater), through novel indicies, could enhance the generalizability of machine learning-based groundwater surface water models (Janssen & Ameli, 2021). Topography-based indices and satellite data, reflecting how landscapes have evolved, can be derived at fine resolution and ultimately can be used to enhance the capabilities of machine learning models. Indices such as height above the nearest drainage or water body (HAND), horizontal distance from the water body, and topographic index turned out to be the most important topography-based drivers of WTD in previous studies (Ågren et al., 2014; Gabrielli et al., 2018; Koch et al., 2019, 2021; Grabs et al., 2009). Distance to hydrogeologically significant features such as alluvial-fan or consolidated rock may also be important (Lopes et al., 2006).

Alternative topography-based indices such as upgradient recharge (Lopes et al., 2006), regional geomorphic indices (G. Ali et al., 2014), convergence index, and river density (Naghibi et al., 2020), could be tried in future machine learning models since they can have emergent process-oriented causal relationships with WTD. For example, Forster and Smith (1988) showed that the WTD pattern is highly sensitive to the concavity or convexity of hillslopes. Certain ecological markers could also be associated with WTD and constraining groundwater models. For example, in Nevada, Lopes et al. (2006) noted that the Greasewood shrub species cannot grow unless the water table is less than 15 meters deep. Further studies on how different species uptake water and in-depth remotely sensed plant location data could revolutionize our knowledge of WTD. With the massive increase in the availability of satellite data, which can capture the groundwater-dependent features on the land surface at a fine spatial-temporal resolution, future works could further leverage these data to enhance the physical realism and overall strength of groundwater models. While the use of a suite of input indices, millions of pixels of data, and emergent constraints could be straightforward for machine learning models (as done in our paper), such information may be difficult to utilize in physically-based models.

The approaches stated in this section could help us inch closer to reliable WTD estimations, but the bottom line is that we need more reliable and trustworthy observations of WTD which are precise and truly representative of the water table at a given place, or at least some additional information which

could guide us on the usefulness of the real observations, such as labelling confined versus unconfined observational wells as was used in our paper (see Section 3.1). Furthermore, future works could incorporate water usage datasets to help predictions follow the natural drivers of WTD while also accounting for or removing pumping biases (Huang et al., 2018; Wada et al., 2014; Hoekstra et al., 2012; Khan et al., 2023; Hofste et al., 2019; Janssen et al., 2021). More importantly, the groundwater modelling community urgently requires extensive global observations at aquifers with different geology located along non-floodplains and particularly steep mountainous regions. Before such data becomes available, all water table depth predictions should be regarded as educated guesses.

6 Conclusions

In this paper, three physically constrained machine learning model setups were developed to simulate 500 m resolution static WTD across the United States and Canada by sequentially adding more than 12 million proxy observations of WTD to 9 million real observations of WTD. In the first model setup (V1), only real observations of WTD were used to train the XGBoost machine learning algorithm. In V2, in addition to real observations of WTD, close to 12 million proxy observations along the shorelines of surface water bodies were used to train the XGBoost algorithm. Finally, in the third model setup (V3), more than 700,000 DEM-based proxy observations, which could roughly reflect WTD in mountainous landscapes, were added to the previous set of real and proxy observations in order to train the XGBoost algorithm. The spatial pattern of the three machine learning-based simulations of WTD, as well as three existing physically-based (Darcy-based) simulations of WTD, were compared against each other and evaluated against unseen (i.e. not used for model training) real and proxy observations. These comparisons and evaluations were made across the entire study region and within ten major ecoregions of North America to determine where these six simulations corroborate each other's conclusions and where each simulation followed currently available observations.

We found that V1 and V2 could reasonably simulate unseen real observations of WTD, and V2 and V3 could reasonably simulate unseen locations of permanently wet surface waterbodies in most of North America's ecoregions. All six machine-learning and physically-based simulations performed poorly in predicting WTD along the most arid and/or high-elevation ecoregions. The three physically-based simulations, in general, showed weaker performance than machine learning simulations in most ecoregions. Pixel-by-pixel comparisons of all six simulations showed that the three physically-based models provided vastly different simulations of WTD when compared to each other and V1/V2. V3, on the other hand, closely followed the overall patterns of the three physically-based simulations while reasonably matching proxy and real observations of WTD. Opening the black box of our three machine learning model setups showed that V3 strongly followed classical groundwater-surface water interaction models due to topographic index strongly controlling the spatial pattern of V3 predictions, particularly at the local scale.

Regardless of our extensive evaluation against unseen real and proxy observations, and our fairly promising results using physically constrained machine learning algorithms, we remain skeptical of all currently available WTD simulations. Physically (Darcy) based models heavily rely on many improper assumptions and uncertain inputs, while machine learning models hopelessly follow potentially biased observations. Crucially, the verifiability of new, potentially promising models remains limited by our incomplete grasp of groundwater processes at large pixel scales and the pervasive influence of deeply ingrained observational biases. Yet, we remain optimistic given several future directions, including developing novel emergent indices, incorporating more carefully taken and processed observations, and gaining new insights from carefully controlled experiments.

Acknowledgments
The interactive pixel-by-pixel maps of the three machine learning simulations of WTD, developed in this study, can be found at: `https://hgs4wm.eoas.ubc.ca/products`. We thank Scott Jasechko for his constructive comments. The WTD simulation data from de Graaf et al. (2015) is publicly available at `https://datacommons.cyverse.org/browse/iplant/home/shared/commons_repo/curated/DeGraaf_data_comparison_lateral_groundwater_flows_2022`. The WTD simulation data from R. M. Maxwell and Condon (2016) is publicly available in the supplementary material at `https://www.science.org/doi/abs/10.1126/`

science.aaf7891. We thank Ying Fan for providing us with the WTD simulations from Fan et al. (2013). Joseph Janssen contributed to conceptualization, data curation, formal analysis, investigation, methodology, software, validation, visualization, writing - original draft, and writing- review & editing. Ardalan Tootchi contributed to conceptualization, data curation, formal analysis, investigation, validation, visualization, and writing- review & editing. Ali Ameli contributed to conceptualization, writing- review & editing, supervision, and funding acquisition. This work was supported by the Environmental and Climate Change Canada grant awarded to Ali Ameli and the Canadian Statistical Sciences Institute (CANSSI) grant awarded to Ali Ameli. Joseph Janssen also received the Government of Canada's NSERC PhD Scholarship. All data is available upon request and the code is available at https://github.com/HydroML/WTD.

Appendix A Canadian well reports

A1 Quebec

Data was downloaded from the *Données Quebec* database. This database is titled as the hydrogeological database. It includes all documented well drillings across the province. It included no attributed or information classifying the producing aquifer type (confined/unconfined). Similar to many other datasets, Quebec's hydrogeological dataset represents the static level and does not include any indication on current water use of wells.

A2 Ontario

Groundwater and water table depth data was downloaded from WWIS2 database. The Static Water Level attribute in WWIS2 is chosen to signify the depth of the water table. The database encompasses various features of the well of record, including casing depths, water found depth, static level, and some details regarding pumping tests.

A3 Nova Scotia

Nova Scotia's Well Logs were acquired from the Government of Nova Scotia Government website. Most of the info was accessed through the *Department of Environment and Climate Change* and the *Department of Natural Resources and Renewables* web pages. These databases include Well depths, casing, bedrock depth, statics water level, yield, water use and information on location and driller company. To focus on unconfined aquifer well readings, wells with static water level deeper than bedrock were excluded.

A4 Alberta

Groundwater database for the Alberta Province was acquired from the Government of Alberta web page and *Interactive GIS Platform*. A large number of wells with static water level of zero were masked out. These consist almost 170,000 of wells in the Alberta dataset. Most of them have no information on drilled depth or perforation depth. Among these wells (WTD=0) Only those for which the drilled depth and perforation depths were also documented as zero. It consists around 30,000 wells out of 280,000 wells in the provincial database.

A5 British Columbia

Water table depth across the British Columbian was extracted from the *BC Groundwater Database*. The database is in Excel format and it includes information on water use, total drilled depths, casing depths and diameter, bedrock depths, static water level, artesian flows (where available), and many more. Static water levels were filtered for depths below 100 meter, and static water levels deeper than bedrock depths. Also, wells with artesian flow were also excluded.

A6 Saskatchewan

Groundwater database was acquired through direct correspondences with Water Security Agency. Depths were converted from ft to m. Similar to Nova Scotia, flowing wells as well as those with static water levels shallower than screening depths were assumed to be located in confined aquifers and therefore masked out .

A7 New Brunswick

The New Brunswick *Groundwater Level Dataset* was accessed to extract WTD observations. This dataset was in Excel format and includes different attributes such as water use, pumping test data, drilled depth as well as the Initial Water Depth (IWD), bedrock depth, and several more. The IWD was assumed to represent the static water level. Wells with IWDs deeper than bedrock depth were excluded as they were assumed to be in confined aquifers..

A8 NewFoundland and Labrador

Based on correspondence with Government of The Newfoundland and Labrador (NL), the NL does not keep and update a database of the groundwater levels. Data on static water levels across the Province were downloaded from the *GIN database*

A9 Manitoba

Manitoba's Department of Environment was contacted to inquire about documented Provincial datasets. The groundwater dataset, however, was not accessible for public use. As a result, all available *GIN database* in Manitoba was downloaded and used for the study.

A10 Yukon

Similar to a few other provinces and territories, groundwater level data across the Yukon territory was accessed and downloaded from the *GIN database*.

References

Abatzoglou, J. T., Dobrowski, S. Z., Parks, S. A., & Hegewisch, K. C. (2018). Terraclimate, a high-resolution global dataset of monthly climate and climatic water balance from 1958–2015. *Scientific data*, *5*(1), 1–12.

Ågren, A., Lidberg, W., Strömgren, M., Ogilvie, J., & Arp, P. (2014). Evaluating digital terrain indices for soil wetness mapping–a swedish case study. *Hydrology and Earth System Sciences*, *18*(9), 3623–3634.

Ali, G., Birkel, C., Tetzlaff, D., Soulsby, C., McDonnell, J. J., & Tarolli, P. (2014). A comparison of wetness indices for the prediction of observed connected saturated areas under contrasting conditions. *Earth Surface Processes and Landforms*, *39*(3), 399–413.

Ali, G. A., L'Heureux, C., Roy, A. G., Turmel, M.-C., & Courchesne, F. (2011). Linking spatial patterns of perched groundwater storage and stormflow generation processes in a headwater forested catchment. *Hydrological Processes*, *25*(25), 3843–3857.

Allen, R. G., Pereira, L. S., Raes, D., Smith, M., et al. (1998). Crop evapotranspiration-guidelines for computing crop water requirements-fao irrigation and drainage paper 56. *Fao, Rome*, *300*(9), D05109.

Ameli, A. A., & Craig, J. R. (2014). Semianalytical series solutions for three-dimensional groundwater-surface water interaction. *Water Resources Research*, *50*(5), 3893–3906.

Ameli, A. A., & Creed, I. F. (2017). Quantifying hydrologic connectivity of wetlands to surface water systems. *Hydrology and Earth System Sciences*, *21*(3), 1791–1808.

Ameli, A. A., & Creed, I. F. (2019). Groundwaters at risk: wetland loss changes sources, lengthens pathways, and decelerates rejuvenation of groundwater resources. *JAWRA Journal of the*

American Water Resources Association, *55*(2), 294–306.

Bartley, C., Liu, W., & Reynolds, M. (2019). Enhanced random forest algorithms for partially monotone ordinal classification. In *Proceedings of the aaai conference on artificial intelligence* (Vol. 33, pp. 3224–3231).

Ben-David, A., Sterling, L., & Tran, T. (2009). Adding monotonicity to learning algorithms may impair their accuracy. *Expert Systems with Applications*, *36*(3), 6627–6634.

Ben-Salem, N., Reinecke, R., Copty, N. K., Gómez-Hernández, J. J., Varouchakis, E. A., Karatzas, G. P., ... Jomaa, S. (2023). Mapping steady-state groundwater levels in the mediterranean region: The iberian peninsula as a benchmark. *Journal of Hydrology*, 130207.

Beven, K. (1987). Towards a new paradigm in hydrology. in: Water for the future: 506 hydrology in perspective. *IAHS Publication*, *164*, 507.

Beven, K. (1989). Changing ideas in hydrology—the case of physically-based models. *Journal of hydrology*, *105*(1-2), 157–172.

Beven, K. (1993). Prophecy, reality and uncertainty in distributed hydrological modelling. *Advances in water resources*, *16*(1), 41–51.

Beven, K. (2002). Towards a coherent philosophy for modelling the environment. *Proceedings of the royal society of London. Series A: mathematical, physical and engineering sciences*, *458*(2026), 2465–2484.

Beven, K. J., & Kirkby, M. J. (1979). A physically based, variable contributing area model of basin hydrology/un modèle à base physique de zone d'appel variable de l'hydrologie du bassin versant. *Hydrological sciences journal*, *24*(1), 43–69.

Beven, K. J., Kirkby, M. J., Freer, J. E., & Lamb, R. (2021). A history of topmodel. *Hydrology and Earth System Sciences*, *25*(2), 527–549.

Bilolikar, D. K., More, A., Gong, A., & Janssen, J. (2023). How to out-perform default random forest regression: choosing hyperparameters for applications in large-sample hydrology. *arXiv preprint arXiv:2305.07136*.

Boerman, T. C. (2022). *Comparing machine learning models and physics-based models in groundwater science* (Unpublished doctoral dissertation).

Breiman, L. (2001). Random forests. *Machine learning*, *45*(1), 5–32.

Brooks, P. D., Chorover, J., Fan, Y., Godsey, S. E., Maxwell, R. M., McNamara, J. P., & Tague, C. (2015). Hydrological partitioning in the critical zone: Recent advances and opportunities for developing transferable understanding of water cycle dynamics. *Water Resources Research*, *51*(9), 6973–6987.

Cano, J.-R., Gutiérrez, P. A., Krawczyk, B., Woźniak, M., & García, S. (2019). Monotonic classification: An overview on algorithms, performance measures and data sets. *Neurocomputing*, *341*, 168–182.

Chen, J., Sudicky, E., Davison, J., Frey, S., Park, Y.-J., Hwang, H.-T., ... others (2020). Towards a climate-driven simulation of coupled surface-subsurface hydrology at the continental scale: a canadian example. *Canadian Water Resources Journal/Revue canadienne des ressources hydriques*, *45*(1), 11–27.

Chen, T., & Guestrin, C. (2016). Xgboost: A scalable tree boosting system. In *Proceedings of the 22nd acm sigkdd international conference on knowledge discovery and data mining* (pp. 785–794).

Chen, T., He, T., Benesty, M., & Khotilovich, V. (2019). Package 'xgboost'. *R version*, *90*, 1–66.

Condon, L. E., Kollet, S., Bierkens, M. F., Fogg, G. E., Maxwell, R. M., Hill, M. C., ... others (2021). Global groundwater modeling and monitoring: Opportunities and challenges. *Water Resources Research*, *57*(12), e2020WR029500.

Condon, L. E., Markovich, K. H., Kelleher, C. A., McDonnell, J. J., Ferguson, G., & McIntosh, J. C. (2020). Where is the bottom of a watershed? *Water Resources Research*, *56*(3), e2019WR026010.

Cooper, D. J., D'amico, D. R., & Scott, M. L. (2003). Physiological and morphological response patterns of populus deltoides to alluvial groundwater pumping. *Environmental Management*, *31*(2), 0215–0226.

Daac, L. (2004). Global 30 arc-second elevation data set gtopo30. *Land process distributed active archive center*, *20*.

Dai, Y., Xin, Q., Wei, N., Zhang, Y., Shangguan, W., Yuan, H., ... Lu, X. (2019). A global high-resolution data set of soil hydraulic and thermal properties for land surface modeling. *Journal of Advances in Modeling Earth Systems*, *11*(9), 2996–3023.

DeFries, R., & Eshleman, K. N. (2004). Land-use change and hydrologic processes: a major focus for the future. *Hydrological processes*, *18*(11), 2183–2186.

de Graaf, I. d., Sutanudjaja, E., Van Beek, L., & Bierkens, M. (2015). A high-resolution global-scale groundwater model. *Hydrology and Earth System Sciences*, *19*(2), 823–837.

De Graaf, I. E., & Stahl, K. (2022). A model comparison assessing the importance of lateral groundwater flows at the global scale. *Environmental Research Letters*, *17*(4), 044020.

de Graaf, I. E., van Beek, R. L., Gleeson, T., Moosdorf, N., Schmitz, O., Sutanudjaja, E. H., & Bierkens, M. F. (2017). A global-scale two-layer transient groundwater model: Development and application to groundwater depletion. *Advances in water Resources*, *102*, 53–67.

Desbarats, A., Logan, C., Hinton, M., & Sharpe, D. (2002). On the kriging of water table elevations using collateral information from a digital elevation model. *Journal of Hydrology*, *255*(1-4), 25–38.

Detty, J., & McGuire, K. J. (2010). Threshold changes in storm runoff generation at a till-mantled headwater catchment. *Water Resources Research*, *46*(7).

Dong, Y., Qiu, L., Lu, C., Song, L., Ding, Z., Yu, Y., & Chen, G. (2022). A data-driven model for predicting initial productivity of offshore directional well based on the physical constrained extreme gradient boosting (xgboost) trees. *Journal of Petroleum Science and Engineering*, *211*, 110176.

Elçi, A., Flach, G. P., & Molz, F. J. (2003). Detrimental effects of natural vertical head gradients on chemical and water level measurements in observation wells: identification and control. *Journal of Hydrology*, *281*(1-2), 70–81.

Fallah Tehrani, A., Cheng, W., Dembczyński, K., & Hüllermeier, E. (2012). Learning monotone non-linear models using the choquet integral. *Machine Learning*, *89*(1), 183–211.

Fan, Y., Li, H., & Miguez-Macho, G. (2013). Global patterns of groundwater table depth. *Science*, *339*(6122), 940–943.

Fang, K., Ji, X., Shen, C., Ludwig, N., Godfrey, P., Mahjabin, T., & Doughty, C. (2019). Combining a land surface model with groundwater model calibration to assess the impacts of groundwater pumping in a mountainous desert basin. *Advances in Water Resources*, *130*, 12–28.

Flickinger, A. K., & Mitchell, A. C. (2020). *Water-table elevation maps for 2008 and 2016 and water-table elevation changes in the aquifer system underlying eastern albuquerque, new mexico* (Tech. Rep.). US Geological Survey.

Forster, C., & Smith, L. (1988). Groundwater flow systems in mountainous terrain: 2. controlling factors. *Water Resources Research*, *24*(7), 1011–1023.

Freeze, R. A., & Cherry, J. A. (1979). *Groundwater*. Upper Saddle River, NJ 07458: Prentice Hall, Inc.

Freund, E. R., Seybold, H., Jasechko, S., & Kirchner, J. W. (2023). Groundwater's fingerprint in stream network branching angles. *Geophysical Research Letters*, *50*(19), e2023GL103599.

Gabrielli, C., Morgenstern, U., Stewart, M., & McDonnell, J. (2018). Contrasting groundwater and streamflow ages at the maimai watershed. *Water Resources Research*, *54*(6), 3937–3957.

Gallant, A. L. (1989). *Regionalization as a tool for managing environmental resources* (Vol. 600) (No. 3-60). US Environmental Protection Agency, Environmental Research Laboratory.

Gleeson, T., Befus, K. M., Jasechko, S., Luijendijk, E., & Cardenas, M. B. (2016). The global volume and distribution of modern groundwater. *Nature Geoscience*, *9*(2), 161–167.

Gleeson, T., Marklund, L., Smith, L., & Manning, A. H. (2011). Classifying the water table at regional to continental scales. *Geophysical Research Letters*, *38*(5).

Gleeson, T., Moosdorf, N., Hartmann, J., & Van Beek, L. (2014). A glimpse beneath earth's surface: Global hydrogeology maps (glhymps) of permeability and porosity. *Geophysical Research Letters*, *41*(11), 3891–3898.

Gleeson, T., Wagener, T., Döll, P., Zipper, S. C., West, C., Wada, Y., ... others (2021). Gmd perspective: The quest to improve the evaluation of groundwater representation in continental-to global-scale models. *Geoscientific Model Development*, *14*(12), 7545–7571.

Gnann, S., Reinecke, R., Stein, L., Wada, Y., Thiery, W., Müller Schmied, H., ... others (2023).

Functional relationships reveal differences in the water cycle representation of global water models. *Nature Water*, 1–12.

Grabs, T., Seibert, J., Bishop, K., & Laudon, H. (2009). Modeling spatial patterns of saturated areas: A comparison of the topographic wetness index and a dynamic distributed model. *Journal of Hydrology*, *373*(1-2), 15–23.

Grubinger, T., Zeileis, A., & Pfeiffer, K.-P. (2014). evtree: Evolutionary learning of globally optimal classification and regression trees in r. *Journal of statistical software*, *61*, 1–29.

Gutiérrez, P. A., & García, S. (2016). Current prospects on ordinal and monotonic classification. *Progress in Artificial Intelligence*, *5*(3), 171–179.

Hayashi, M., van der Kamp, G., & Rosenberry, D. O. (2016). Hydrology of prairie wetlands: understanding the integrated surface-water and groundwater processes. *Wetlands*, *36*, 237–254.

Herrera, P. A., Langevin, C., & Hammond, G. (2022). Estimation of the water table position in unconfined aquifers with modflow 6. *Groundwater*.

Hilton, A., & Jasechko, S. (2023). Widespread aquifer depressurization after a century of intensive groundwater use in usa. *Science Advances*, *9*(37), eadh2992.

Hinton, M., Schiff, S., & English, M. (1993). Physical properties governing groundwater flow in a glacial till catchment. *Journal of Hydrology*, *142*(1-4), 229–249.

Hoekstra, A. Y., Mekonnen, M. M., Chapagain, A. K., Mathews, R. E., & Richter, B. D. (2012). Global monthly water scarcity: blue water footprints versus blue water availability. *PloS one*, *7*(2), e32688.

Hofste, R. W., Kuzma, S., Walker, S., Sutanudjaja, E. H., Bierkens, M. F., Kuijper, M. J., ... others (2019). Aqueduct 3.0: Updated decision-relevant global water risk indicators. *World Resources Institute*, 1–53.

Huang, Z., Hejazi, M., Li, X., Tang, Q., Vernon, C., Leng, G., ... others (2018). Reconstruction of global gridded monthly sectoral water withdrawals for 1971–2010 and analysis of their spatiotemporal patterns. *Hydrology and Earth System Sciences*, *22*(4), 2117–2133.

Istalkar, P., Kadu, A., & Biswal, B. (2023). Value of process understanding in the era of machine learning: A case for recession flow prediction. *Journal of Hydrology*, 130350. Retrieved from `https://www.sciencedirect.com/science/article/pii/S0022169423012921` doi: https://doi.org/10.1016/j.jhydrol.2023.130350

James, G., Witten, D., Hastie, T., & Tibshirani, R. (2013). *An introduction to statistical learning* (Vol. 112). Springer.

Janssen, J., & Ameli, A. A. (2021). A hydrologic functional approach for improving large-sample hydrology performance in poorly gauged regions. *Water Resources Research*, *57*(9), e2021WR030263.

Janssen, J., Guan, V., & Robeva, E. (2023). Ultra-marginal feature importance: Learning from data with causal guarantees. In *International conference on artificial intelligence and statistics* (pp. 10782–10814).

Janssen, J., Radić, V., & Ameli, A. (2021). Assessment of future risks of seasonal municipal water shortages across north america. *Frontiers in Earth Science*, *9*, 730631.

Jasechko, S., & Perrone, D. (2020). California's central valley groundwater wells run dry during recent drought. *Earth's Future*, *8*(4), e2019EF001339.

Jasechko, S., Seybold, H., Perrone, D., Fan, Y., & Kirchner, J. W. (2021). Widespread potential loss of streamflow into underlying aquifers across the usa. *Nature*, *591*(7850), 391–395.

Jasechko, S., Seybold, H., Perrone, D., Fan, Y., Shamsudduha, M., Taylor, R. G., ... Kirchner, J. W. (2024). Rapid groundwater decline and some cases of recovery in aquifers globally. *Nature*, *625*(7996), 715–721.

Karlstrom, L., Grant, G. E., Klema, N., Sullivan, P. L., Cooley, S. W., Fasthe, B., & Cashman, K. V. (2023). State shifts in the deep critical zone drive landscape evolution in volcanic terrains. *AGU23*.

Ke, G., Meng, Q., Finley, T., Wang, T., Chen, W., Ma, W., ... Liu, T.-Y. (2017). Lightgbm: A highly efficient gradient boosting decision tree. *Advances in neural information processing systems*, *30*.

Khan, Z., Thompson, I., Vernon, C. R., Graham, N. T., Wild, T. B., & Chen, M. (2023). Global monthly sectoral water use for 2010–2100 at 0.5° resolution across alternative futures. *Scientific*

Data, *10*(1), 201.

Kibler, C. L., Schmidt, E. C., Roberts, D. A., Stella, J. C., Kui, L., Lambert, A. M., & Singer, M. B. (2021). A brown wave of riparian woodland mortality following groundwater declines during the 2012–2019 california drought. *Environmental Research Letters*, *16*(8), 084030.

Kim, H. J., Sidle, R. C., Moore, R., & Hudson, R. (2004). Throughflow variability during snowmelt in a forested mountain catchment, coastal british columbia, canada. *Hydrological Processes*, *18*(7), 1219–1236.

Kirchner, J. W. (2006). Getting the right answers for the right reasons: Linking measurements, analyses, and models to advance the science of hydrology. *Water resources research*, *42*(3).

Klemes, V., et al. (1982). Empirical and causal models in hydrology. *Scientific basis of water resource management*, 95–104.

Koch, J., Berger, H., Henriksen, H. J., & Sonnenborg, T. O. (2019). Modelling of the shallow water table at high spatial resolution using random forests. *Hydrology and Earth System Sciences*, *23*(11), 4603–4619.

Koch, J., Gotfredsen, J., Schneider, R., Troldborg, L., Stisen, S., & Henriksen, H. J. (2021). High resolution water table modeling of the shallow groundwater using a knowledge-guided gradient boosting decision tree model. *Frontiers in Water*, 81.

Koirala, S., Yeh, P. J.-F., Hirabayashi, Y., Kanae, S., & Oki, T. (2014). Global-scale land surface hydrologic modeling with the representation of water table dynamics. *Journal of Geophysical Research: Atmospheres*, *119*(1), 75–89.

Kollet, S. J., & Maxwell, R. M. (2008). Capturing the influence of groundwater dynamics on land surface processes using an integrated, distributed watershed model. *Water Resources Research*, *44*(2).

Li, H., & Ameli, A. A. (2023). Upland hillslope groundwater subsidy affects low-flow storage–discharge relationship. *Water Resources Research*, *59*(10), e2022WR034155.

Liu, X., Han, X., Zhang, N., & Liu, Q. (2020). Certified monotonic neural networks. *Advances in Neural Information Processing Systems*, *33*, 15427–15438.

Lopes, T. J., Buto, S. G., Smith, J., & Welborn, T. L. (2006). *Water-table levels and gradients, nevada, 1947-2004* (Vol. 2006). US Department of the Interior, US Geological Survey.

Ma, Y., Leonarduzzi, E., Defnet, A., Melchior, P., Condon, L. E., & Maxwell, R. M. (2024). Water table depth estimates over the contiguous united states using a random forest model. *Groundwater*, *62*(1), 34–43.

Manning, A. H., Verplanck, P. L., Caine, J. S., & Todd, A. S. (2013). Links between climate change, water-table depth, and water chemistry in a mineralized mountain watershed. *Applied geochemistry*, *37*, 64–78.

Marthews, T., Dadson, S., Lehner, B., Abele, S., & Gedney, N. (2015). High-resolution global topographic index values for use in large-scale hydrological modelling. *Hydrology and Earth System Sciences*, *19*(1), 91–104.

Maxwell, R., Condon, L., & Kollet, S. (2015). A high-resolution simulation of groundwater and surface water over most of the continental us with the integrated hydrologic model parflow v3. *Geoscientific model development*, *8*(3), 923–937.

Maxwell, R. M., & Condon, L. E. (2016). Connections between groundwater flow and transpiration partitioning. *Science*, *353*(6297), 377–380.

Messager, M. L., Lehner, B., Grill, G., Nedeva, I., & Schmitt, O. (2016). Estimating the volume and age of water stored in global lakes using a geo-statistical approach. *Nature communications*, *7*(1), 13603.

Miguez-Macho, G., & Fan, Y. (2012). The role of groundwater in the amazon water cycle: 1. influence on seasonal streamflow, flooding and wetlands. *Journal of Geophysical Research: Atmospheres*, *117*(D15).

Minnig, M., Moeck, C., Radny, D., & Schirmer, M. (2018). Impact of urbanization on groundwater recharge rates in dübendorf, switzerland. *Journal of Hydrology*, *563*, 1135–1146.

Moeck, C., Grech-Cumbo, N., Podgorski, J., Bretzler, A., Gurdak, J. J., Berg, M., & Schirmer, M. (2020). A global-scale dataset of direct natural groundwater recharge rates: A review of variables, processes and relationships. *Science of the total environment*, *717*, 137042.

Mohan, C., Western, A. W., Wei, Y., & Saft, M. (2018). Predicting groundwater recharge for varying

land cover and climate conditions–a global meta-study. *Hydrology and Earth System Sciences*, *22*(5), 2689–2703.

Molénat, J., Gascuel-Odoux, C., Davy, P., & Durand, P. (2005). How to model shallow water-table depth variations: The case of the kervidy-naizin catchment, france. *Hydrological Processes: An International Journal*, *19*(4), 901–920.

Moreno, H., Gupta, H., White, D., & Sampson, D. (2015). Modeling the distributed effects of forest thinning on the long-term water balance and stream flow extremes for a semi-arid basin in the southwestern us. *Hydrology & Earth System Sciences Discussions*, *12*(10).

Naghibi, S. A., Hashemi, H., Berndtsson, R., & Lee, S. (2020). Application of extreme gradient boosting and parallel random forest algorithms for assessing groundwater spring potential using dem-derived factors. *Journal of Hydrology*, *589*, 125197.

Nearing, G. S., Kratzert, F., Sampson, A. K., Pelissier, C. S., Klotz, D., Frame, J. M., ... Gupta, H. V. (2021). What role does hydrological science play in the age of machine learning? *Water Resources Research*, *57*(3), e2020WR028091.

Nobre, A. D., Cuartas, L. A., Hodnett, M., Rennó, C. D., Rodrigues, G., Silveira, A., & Saleska, S. (2011). Height above the nearest drainage–a hydrologically relevant new terrain model. *Journal of Hydrology*, *404*(1-2), 13–29.

Ofterdinger, U., Renard, P., & Loew, S. (2014). Hydraulic subsurface measurements and hydrodynamic modelling as indicators for groundwater flow systems in the rotondo granite, central alps (switzerland). *Hydrological Processes*, *28*(2), 255–278.

Omernik, J. M. (1987). Ecoregions of the conterminous united states. *Annals of the Association of American geographers*, *77*(1), 118–125.

Osman, A. I. A., Ahmed, A. N., Chow, M. F., Huang, Y. F., & El-Shafie, A. (2021). Extreme gradient boosting (xgboost) model to predict the groundwater levels in selangor malaysia. *Ain Shams Engineering Journal*, *12*(2), 1545–1556.

Ovchinnik, S., Otero, F. E., & Freitas, A. A. (2019). Monotonicity detection and enforcement in longitudinal classification. In *International conference on innovative techniques and applications of artificial intelligence* (pp. 63–77).

Owuor, S. O., Butterbach-Bahl, K., Guzha, A. C., Rufino, M. C., Pelster, D. E., Díaz-Pinés, E., & Breuer, L. (2016). Groundwater recharge rates and surface runoff response to land use and land cover changes in semi-arid environments. *Ecological Processes*, *5*, 1–21.

Pekel, J.-F., Cottam, A., Gorelick, N., & Belward, A. S. (2016). High-resolution mapping of global surface water and its long-term changes. *Nature*, *540*(7633), 418–422.

Poggio, L., De Sousa, L. M., Batjes, N. H., Heuvelink, G., Kempen, B., Ribeiro, E., & Rossiter, D. (2021). Soilgrids 2.0: producing soil information for the globe with quantified spatial uncertainty. *Soil*, *7*(1), 217–240.

Probst, P., Boulesteix, A.-L., & Bischl, B. (2019). Tunability: Importance of hyperparameters of machine learning algorithms. *The Journal of Machine Learning Research*, *20*(1), 1934–1965.

Prokhorenkova, L., Gusev, G., Vorobev, A., Dorogush, A. V., & Gulin, A. (2018). Catboost: unbiased boosting with categorical features. *Advances in neural information processing systems*, *31*.

Rasmussen, T. C., & Crawford, L. A. (1997). Identifying and removing barometric pressure effects in confined and unconfined aquifers. *Groundwater*, *35*(3), 502–511.

Reinecke, R., Foglia, L., Mehl, S., Herman, J. D., Wachholz, A., Trautmann, T., & Döll, P. (2019). Spatially distributed sensitivity of simulated global groundwater heads and flows to hydraulic conductivity, groundwater recharge, and surface water body parameterization. *Hydrology and Earth System Sciences*, *23*(11), 4561–4582.

Reinecke, R., Foglia, L., Mehl, S., Trautmann, T., Cáceres, D., & Döll, P. (2019). Challenges in developing a global gradient-based groundwater model (g 3 m v1. 0) for the integration into a global hydrological model. *Geoscientific Model Development*, *12*(6), 2401–2418.

Reinecke, R., Gnann, S., Stein, L., Bierkens, M., de Graaf, I., Gleeson, T., ... others (2023). Global accessibility of groundwater remains highly uncertain.

Reinecke, R., Wachholz, A., Mehl, S., Foglia, L., Niemann, C., & Döll, P. (2020). Importance of spatial resolution in global groundwater modeling. *Groundwater*, *58*(3), 363–376.

Rust, W., Holman, I., Bloomfield, J., Cuthbert, M., & Corstanje, R. (2019). Understanding the po-

tential of climate teleconnections to project future groundwater drought. *Hydrology and Earth System Sciences*, *23*(8), 3233–3245.

Scaini, A., Hissler, C., Fenicia, F., Juilleret, J., Iffly, J. F., Pfister, L., & Beven, K. (2018). Hillslope response to sprinkling and natural rainfall using velocity and celerity estimates in a slate-bedrock catchment. *Journal of Hydrology*, *558*, 366–379.

Scanlon, B. R., Reedy, R. C., Stonestrom, D. A., Prudic, D. E., & Dennehy, K. F. (2005). Impact of land use and land cover change on groundwater recharge and quality in the southwestern us. *Global Change Biology*, *11*(10), 1577–1593.

Schook, D. M., Friedman, J. M., Hoover, J. D., Rice, S. E., Thaxton, R. D., & Cooper, D. J. (2022). Riparian forest productivity decline initiated by streamflow diversion then amplified by atmospheric drought 40 years later. *Ecohydrology*, *15*(3), e2408.

Seibert, J. (2003). Reliability of model predictions outside calibration conditions: Paper presented at the nordic hydrological conference (røros, norway 4-7 august 2002). *Hydrology Research*, *34*(5), 477–492.

Shwartz-Ziv, R., & Armon, A. (2022). Tabular data: Deep learning is not all you need. *Information Fusion*, *81*, 84–90.

Siebert, S., Burke, J., Faures, J.-M., Frenken, K., Hoogeveen, J., Döll, P., & Portmann, F. T. (2010). Groundwater use for irrigation–a global inventory. *Hydrology and earth system sciences*, *14*(10), 1863–1880.

Silliman, S., & Mantz, G. (2000). The effect of measurement error on estimating the hydraulic gradient in three dimensions. *Groundwater*, *38*(1), 114–120.

Sivapalan, M., & Kalma, J. D. (1995). Scale problems in hydrology: Contributions of the robertson workshop. *Hydrological Processes*, *9*(3-4), 243–250.

Smerdon, B., Allen, D., Grasby, S., & Berg, M. (2009). An approach for predicting groundwater recharge in mountainous watersheds. *Journal of Hydrology*, *365*(3-4), 156–172.

Smith, R. G., & Majumdar, S. (2020). Groundwater storage loss associated with land subsidence in western united states mapped using machine learning. *Water Resources Research*, *56*(7), e2019WR026621.

Somers, L. D., McKenzie, J. M., Mark, B. G., Lagos, P., Ng, G.-H. C., Wickert, A. D., ... Silva, Y. (2019). Groundwater buffers decreasing glacier melt in an andean watershed—but not forever. *Geophysical Research Letters*, *46*(22), 13016–13026.

Tai, X., Mackay, D. S., Sperry, J. S., Brooks, P., Anderegg, W. R., Flanagan, L. B., ... Hopkinson, C. (2018). Distributed plant hydraulic and hydrological modeling to understand the susceptibility of riparian woodland trees to drought-induced mortality. *Water Resources Research*, *54*(7), 4901–4915.

Tang, G., Clark, M. P., Papalexiou, S. M., Newman, A. J., Wood, A. W., Brunet, D., & Whitfield, P. H. (2021). Emdna: An ensemble meteorological dataset for north america. *Earth System Science Data*, *13*(7), 3337–3362.

Tozer, B., Sandwell, D. T., Smith, W. H., Olson, C., Beale, J., & Wessel, P. (2019). Global bathymetry and topography at 15 arc sec: Srtm15+. *Earth and Space Science*, *6*(10), 1847–1864.

Tran, H., Zhang, J., O'Neill, M. M., Ryken, A., Condon, L. E., & Maxwell, R. M. (2022). A hydrological simulation dataset of the upper colorado river basin from 1983 to 2019. *Scientific Data*, *9*(1), 1–17.

Tyralis, H., Papacharalampous, G., & Langousis, A. (2019). A brief review of random forests for water scientists and practitioners and their recent history in water resources. *Water*, *11*(5), 910.

Vaheddoost, B., & Aksoy, H. (2018). Interaction of groundwater with lake urmia in iran. *Hydrological processes*, *32*(21), 3283–3295.

van Meerveld, I. (2024). *The (ir) relevance of plot-and hillslope scale processes for catchment runoff* (Tech. Rep.). Copernicus Meetings.

Vincent, E., Post, A., & von Asmuth, J. R. (2013). Hydraulic head measurements–new technologies, classic pitfalls. *Hydrogeology Journal*, *21*(4), 737.

Wada, Y., Wisser, D., & Bierkens, M. F. (2014). Global modeling of withdrawal, allocation and consumptive use of surface water and groundwater resources. *Earth System Dynamics*, *5*(1), 15–40.

Xu, G., Mi, X.-J., Ma, J., Ma, J., & Tang, L.-S. (2022). Impact of groundwater depth on hydraulic performance and growth of haloxylon ammodendron in a desert region of central asia. *Ecohydrology*, *15*(5), e2394.

Xu, S., Frey, S., Erler, A., Khader, O., Berg, S., Hwang, H., ... Sudicky, E. (2021). Investigating groundwater-lake interactions in the laurentian great lakes with a fully-integrated surface water-groundwater model. *Journal of Hydrology*, *594*, 125911.

Yamazaki, D., Ikeshima, D., Sosa, J., Bates, P. D., Allen, G. H., & Pavelsky, T. M. (2019). Merit hydro: a high-resolution global hydrography map based on latest topography dataset. *Water Resources Research*, *55*(6), 5053–5073.

Yang, Y., & Chui, T. F. M. (2021). Reliability assessment of machine learning models in hydrological predictions through metamorphic testing. *Water Resources Research*, *57*(9), e2020WR029471.

Zhang, Y.-K., & Schilling, K. (2006). Effects of land cover on water table, soil moisture, evapotranspiration, and groundwater recharge: a field observation and analysis. *Journal of Hydrology*, *319*(1-4), 328–338.